Implementation of User Element Subroutines for Frequency Domain Analysis of Wave Scattering Problems with Commercial Finite Element Codes

Felipe Mosquera-Arias
lmosquer@eafit.edu.co

Grupo de Mecánica Aplicada
Departamento de Ingeniería Civil
Escuela de Ingeniería
Universidad EAFIT
Medellín, Colombia
2013

Implementation of User Element Subroutines for Frequency Domain Analysis of Wave Scattering Problems with Commercial Finite Element Codes

Felipe Mosquera-Arias
lmosquer@eafit.edu.co

A thesis submitted to the
Faculty of the Civil Engineering Department
Universidad EAFIT
in partial fulfillment of the requirements for the degree of
Master of Science

Departamento de Ingeniería Civil

Nota de aceptación

Presidente del jurado

Jurado

Jurado

Ciudad y Fecha

Acknowledgements

This project has been conducted with combined financial support between Solingral S.A, Universidad EAFIT research fund and Colciencias.

Table of Contents

List of figures

Abstract

A user element subroutine (UEL) to be used into the commercial finite element code ABAQUS has been developed and implemented. The subroutine is intended to treat generalized wave propagation problems in 2D-domains and in particular wave scattering problems. It has been formulated in the frequency domain, but fully implemented in terms of real-valued degrees of freedom as required by ABAQUS. Results are obtained both in the frequency and time domain. The subroutine is tested in the solution of problems related to topographic effects in earthquake engineering and in the propagation of waves in materials with microstructure introducing dispersion. Results have been provided in the frequency and in the time domain. The frequency domain is not only powerful from a conceptual point of view, since it offers many insights into the physical aspects of the problem, but it also has other advantages like:

- Easy incorporation of excitations based on plane wave assumptions.
- Simultaneous Consideration of temporal and spatial periodicity.
- Easy consideration of dispersive materials.

Keywords: Wave Propagation, Computational Elastodynamics, Finite Element Methods, Boundary Element Methods, Seismic Waves, Periodic Materials.

Introduction

The phenomenon of wave propagation appears in many different engineering fields, e.g., electromagnetism, acoustics, mechanics. At the same time, computational methods have evolved to the point, where simulation based engineering is increasingly being used by the practising engineer in order to support lab results, improve proposed designs or even to compensate for the lack of experimental data. In the case of mechanical waves, the subject is of interest in diverse engineering topics like, earthquake engineering; geophysics; mechanical characterization of materials; and oil and natural gas exploration, among others.

Although computational mechanics based techniques, allow the problem of wave propagation to be solved with great accuracy, the existing commercial tools still pose limitations to the user, due to different factors. For instance, commercial codes are limited in the type of available kinematic assumptions, they only have a few constitutive material models and they are also limited in the possible forms of excitation. These limitations have kept a lot of problems of wave propagation within the strict realm of academics and researchers. One of the major limitations in commercial codes is the impossibility of performing analysis in the frequency domain with enough flexibility in the type of excitation, mainly because most commercial software don't allow the user to pass complex-valued information. This limitation is taken care of in this thesis.

In this work a computational tool for the simulation of generalized wave propagation problems in the commercial finite element code ABAQUS is presented. The computational framework is developed in the form of a user element subroutine (UEL), which is a possibility offered to the user by commercial codes, like ABAQUS, to overcome limitations in the type of analysis implicit in the code. This work has been motivated by a need identified within the Grupo de Mecánica Aplicada at Universidad EAFIT to solve wave propagation problems of moderate size (e.g., in the range of millions of degrees of freedom), when working in the particular context of earthquake engineering.

The subroutine takes advantage of the powerful simulation resources available in the commercial code, like its pre and post-processing units and efficient solvers, allowing the analyst to simulate a complex problem, not available in the code, but with the easiness of data input implicit in a robust commercial software.

Although the current UEL subroutine is developed in the context of earthquake engineering, it

is general enough and straight forward to modify as required, so it can be easily extended to many different applications and physical areas. This generality is possible, since the analysis is conducted in the frequency domain but in terms of real algebra calculations. In this sense ABAQUS is used as a solver for a series of generalized static problems while being unaware of the type of physical problem being solved. The particular implementation uses the idea of generalized variables to proceed in the frequency domain, but expressing the problem in terms of real valued functions. The frequency domain is not only powerful from a conceptual point of view since it offers many insights into the physical aspects of the problem, but it also has other advantages like:

- Easy incorporation of excitations based on plane wave assumptions.
- Simultaneous consideration of temporal and spatial periodicity.
- Easy consideration of dispersive materials.

Although the main objective of this thesis is the formulation and implementation of the UEL subroutine into the commercial FEM code ABAQUS, several problems have been solved in order to test and show the subroutine's current capability. The following problems have been solved:

- Scattering of incident in-plane P waves by surface shapes in a micropolar solid. The scattering of waves by a geometric irregularity embedded in a non-classical material model has been studied in order to simulate a dispersive medium. For this purpose a Cosserat or kinematically enriched material model has been numerically simulated.
- Scattering of incident in-plane P and SV elastic waves by surface scatterers. The context of the analysis corresponds to the problem of topographic effects in earthquake engineering. A method, based on the isolation of the diffracted part of the response has been presented and explored, where the diffraction field is used as a digital finger print of the topographic effect.
- Study of the topographic effects in a simplified model of a sedimentary basin with a cross section resembling the Valle de Aburrá. A domain reduction method has been explored as a potential analysis tool to establish the connection between large geometrical or regional topographic effects and localized mechanical effects like the ones existing in seismic microzones.

The routine capabilities include:

- Plane wave propagation analysis in infinite and semi-infinite domains using absorbing boundaries.

- Point source wave propagation analysis in infinite and semi-infinite domains using absorbing boundaries.
- Simulation of homogeneous and heterogeneous domains.
- Flexibility of boundary conditions like topographies of arbitrary shapes or dams in a strong topographic environment.
- Results in the frequency domain in the form of spatial transfer functions between response and incident motions and in the form of Fourier spectral amplitudes at a given point.
- Results in the time domain in the form of synthetic seismograms at user defined receivers and videos of the propagation patterns inside the complete computational domain.
- Easy consideration of dispersive materials.

The implemented UEL subroutine has been tested in a standard desktop computer with 16Gb of memory. Models as large as 6'000.000 degrees of freedom have been solved. The UEL subroutine and the post-processing software can be downloaded freely from the Mecánica Aplicada web site `http://mecanica.eafit.edu.co/mecanica/`.

This report is organized as follows. In the first chapter the wave scattering problem in elastodynamics is reviewed in differential and integral form. The formulation used by Bielak & Christiano (1984) in terms of total motions inside the scatterer and scattered motions inside the half-space is presented. Chapter 2 describes aspects of the algorithm used in the solution of wave scattering problems within the context of the finite element method (FEM). The idea of generalized variables and a generalized principle of virtual displacements in complex algebra as required by the frequency domain is introduced. The principle is then discretized but treating the real and imaginary parts independently. In this chapter a couple of simple verification problems are solved. Applications of the subroutine start in Chapter 3 with the problem of topographic and site effects in earthquake engineering and continue in Chapter 4 with the diffraction and scattering of waves in a micro-polar half-space. Conclusions and recommendations for further work are presented in the final part.

In the next section we include a brief review of the historical development of numerical methods mainly in earthquake engineering.

Literature Review

The problem of scattering and diffraction of elastic waves by surface or subsurface irregularities of arbitrary shape and in general by objects immersed in a homogeneous medium, finds application in areas like the oil and natural gas industry, the mechanical characterization of rock blocks, the determination of topographic effects in earthquake engineering and the development of non-destructive

mechanical testing techniques among many others.Solutions can be obtained via numerical simulation and where complex combinations of geometry, material properties and boundary conditions can be considered. An extensive amount of work on the subject from the numerical point of view has been conducted during the last 30 years. Moreover, it has has been approached with different techniques depending on the specific type of problem and available computer requirements.

In the case of infinite or semi-infinite media problems-as is the usual scenario in earthquake engineering and geophysics-one of the challenges in the numerical solution, is the proper imposition of radiation boundary conditions. This problem can be dealt with in a very natural way, using integral equations formulations and its discretization in terms of different versions of the boundary element method. In that approach the radiation condition is implicit in the specific problem Green's function. Solutions through different versions of the direct and indirect boundary element method and corresponding to problems in different physical contexts are reported in Wong & Jennings (1975), citesills1978scattering, Sánchez-Sesma & Rosenblueth (1979), Sánchez-Sesma (1983), Dravinski & Mossessian (1987), Zhang & Achenbach (1988), Kawase (1988), Manolis & Beskos (1988), Kawase & Aki (1989), Mossessian & Dravinski (1989), Sánchez-Sesma & Campillo (1991), Kim & Papageorgiou (1993), Papageorgiou & Pei (1998), Janod & Coutant (2000), Iturrarán-Viveros et al. (2005), Sohrabi-Bidar et al. (2010). Although BE-based solutions are very accurate, its effective application to real size problems is very limited due to large computing requirements. As a result, the method is currently being used as a tool to perform parametric analysis in conceptual problems.

The first numerical solutions of wave diffraction problems with full domain methods, combined with absorbing surfaces to represent the radiation condition were obtained in terms of classical finite difference algorithms e.g.,(Boore, 1972; Archuleta & Frazier, 1978; Archuleta & Day, 1980). One of the major drawbacks of finite difference schemes, is the appearance of numerical dispersion near zones of large gradients of the field. Moreover, in large scale simulations–representative of realistic problems–the balancing of the trade-off between numerical dispersion and computational cost, turns out to be rather difficult, Komatitsch & Vilotte (1998). This numerical phenomenon can be avoided using staggered-grid formulations (e.g., (Madariaga, 1977; Virieux, 1986; Levander, 1988; Moczo et al., 2007). Additional works using finite difference schemes, although mainly related to seismic engineering problems, can be identified in Vidale & Helmberger (1988) in the study of surface waves with a 2D model of the Los Angeles basin, Frankel & Vidale (1992) in the response of the Santa Clara Valley to the 1989 Loma Prieta earthquake using one of the first full 3D models, Frankel (1993) in the response of the San Bernardino valley, Graves (1996) with a model of the Marina district in California using staggered grids and similar works like Yomogida & Etgen (1993), Olsen & Archuleta (1996), Stekl & Pratt (1998). Finite difference schemes combined with other techniques to effectively account for free surfaces and general boundary conditions still dominate the spectrum of numerical treatments of wave propagation problems.

A recent comparison of the results obtained with different methods-among which one finds FD's schemes-can be found in Bielak et al. (2010). Almost in parallel to the developments in terms of finite differences, the other domain method that is naturally identified corresponds to the finite

element method. Early solutions to wave propagation problems were reported by Lysmer & Drake (1972), Smith (1975), Ohtsuki & Harumi (1983), Mita & Luco (1987), Toshinawa & Ohmachi (1992). The first large scale simulation with FEM implementations were performed by Bao et al. (1998), who proposed and explicit algorithm embedded into an octree-based data storage scheme allowing for the simulation of real large scale problems; the resulting algorithm however, was restrained to problems without the consideration of topographic effects. These set of algorithms were later improved by Bielak et al. (2003) and Yoshimura et al. (2003), where a domain reduction method that allowed to effectively translate the source effects near the scatterer was proposed and by Bielak et al. (2009), Taborda & Bielak (2010), where problems of frequencies up to 5.0Hz and billions of elements have been solved.

Other recent classical FEM treatments can be found in Aagaard & Heaton (2004), Ma & Liu (2006), Ichimura et al. (2007). The most efficient classical FEM algorithms to study wave propagation at large scales correspond to explicit methods where the equilibrium equations are uncoupled through artificial imposition of lumped mass matrix. Another class of methods that has received much attention during the recent years corresponds to the so-called Spectral Finite Element Methods. These find their origins in the spectral methods originally developed in the context of fluid dynamics, eg., Orszag (1980), and in its later extensions to elastodynamics, Gazdag (1981), Kosloff & Baysal (1982). Improved versions in the form of the early forms of the spectral finite element methods were later proposed by Patera (1984) and Maday & Patera (1989) for fluid problems and byPriolo et al. (1994) and Faccioli et al. (1996) for wave propagation problems. One of the major limitations of these class of methods when dealing with wave propagation problems, was related to the need for non-uniform spacing of the collocation points and strong requirements in the time step. These drawbacks were later removed in the implementations by Komatitsch & Vilotte (1998), Komatitsch & Tromp (1999), Chaljub et al. (2003), Komatitsch et al. (2004), Lee et al. (2010), Lee et al. (2009a), Lee et al. (2009b) and Chaljub et al. (2010).

Chapter 1

The Wave Scattering Problem in Elastodynamics

Introduction

The problem of scattering and diffraction of elastic waves, by mechanical and geometrical irregularities, located over infinite or semi-infinite domains, is relevant in the analysis and design of civil engineering structures subject to seismic events. In particular, there is a strong interest in finding the appropriate design motions, when an incident seismic field interacts with a discontinuity in the form of surface or subsurface topography. In the context of earthquake engineering the problem is termed the site effects problem, while in the more general context of the theory of wave propagation, it is referred to like a scattering problem.

Mathematically, the problem corresponds to an Initial Boundary Value Problem (IVBP) satisfied over a semi-infinite domain and it is defined as follows: If one considers a prescribed incident field, impinging over a geometrically perturbed half-space (that is, a half-space with a discontinuity), the incident motions are modified by the geometrical disturbances, which subsequently become sources of scattered motions. The purpose of the analysis is the determination of the total displacements inside the scatterer and of the scattered motions over the half-space.

In the first part of this chapter, the differential equations representing mechanical equilibrium and the corresponding boundary conditions for the scatterer and the supporting half-space are formulated. The resulting boundary value problems in each domain, are then welded together through displacement and tractions compatibility arguments along their common coupling surface S. This yields a single well-posed BVP for the complete scatterer-half-space system. Considering the full problem, it becomes evident that the half-space plays the roll of a radiation boundary condition for the scatterer, carrying with it the sources and proper support conditions to be

prescribed along the common coupling interface S. This work deals precisely with the imposition of radiation boundary conditions in terms of Half-Space Super Elements (HSSE), that can be incorporated into the scatterer discrete equilibrium equations in a commercial finite element code.

In the second part of the chapter, we formulate the BVP in the alternative form of integral equations, with the aid of the elastodynamics representation theorem. The discrete versions of this alternative formulations give rise to boundary element numerical schemes. As a result, the following discrete approximations would be possible within the context of this work;

- An approximation in terms of a domain of standard finite elements combined with silent boundaries.
- A semi-analytic description in terms of a boundary integral equation for the half-space using the specific half-space Green's function.
- An approximation in terms of a boundary integral equation for the half-space using a full-space Green's function and prescribed incoming motions.

In this work we only implemented the first of the above three approaches but extension to the other two is straight forward.

1.1 Boundary Value Problem Governing the Scattering of Elastic Waves

1.1.1 Differential Formulation

In the analysis that follows, the physically consistent initial boundary value problem, involving space and time derivatives and properly specified, initial and boundary conditions, is cast into a series of equivalent Boundary Value Problems (BVP) using the Fourier transform technique. As a result the wave (or elastodynamics) equations of motion, take the form of the frequency domain reduced wave equations, see Eringen & Şuhubi (1975). For that purpose all the involved variables are assumed to exhibit a time dependence of the form $e^{\hat{i}\omega t}$, where ω represents circular frequency and $\hat{i} = \sqrt{-1}$ is the imaginary unit. At the same time all the variables are assumed to have a complex amplitude at a given point $\vec{x}$ of the general form $\hat{F}(\vec{x}, \hat{i}\omega)$ when a time to frequency transform is performed and of the form $\hat{\hat{F}}(\hat{i}\vec{\kappa}, \hat{i}\omega)$ when both, space and time are transformed. The following sign convention is used for this general space-time Fourier transform:

$$\vec{u}(\vec{x},t) = \int_{-\infty}^{+\infty}\int_{-\infty}^{+\infty} \hat{\vec{U}}(\hat{i}\vec{\kappa},\hat{i}\omega)e^{-\hat{i}\vec{k}\cdot\vec{x}}d\vec{\kappa}e^{\hat{i}\omega t}d\omega.$$

The reduced wave equation is now derived with reference to Figure 1.1 where we display an arbitrary geometrical disturbance, (termed herein the scatterer), occupying a volume V_1 and resting on top of a homogeneous elastic surrounding (half-space), occupying a volume V_0. By a mechanical disturbance we mean the change in mechanical properties in the half-space from $(\rho_0, \lambda_0, \mu_0)$ to those in the scatterer $(\rho_1, \lambda_1, \mu_1)$ through the internal surface S perfectly coupling the half-space to the scatterer. Each medium is characterized by its mass density ρ and Lamé constants λ and μ. In elastodynamics however a more appealing definition of a medium is through its SV and P wave propagation velocities defined like $\beta = \sqrt{\mu/\rho}$ and $\alpha = \sqrt{(\lambda+2\mu)/\rho}$. The domain definitions are completed by the exterior normal vectors $\hat{n}$ and $\hat{n^*}$ to the scatterer and half-space respectively.

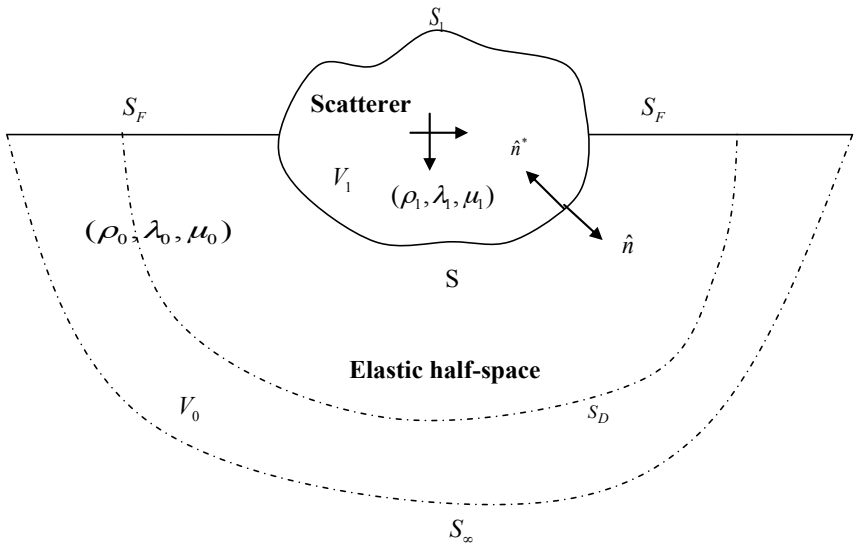

Figure 1.1. Schematic description of the scattering problem.

Let the complete scatterer-half-space system, be subjected to an incident plane wave forming an angle θ with the vertical and assumed to be generated by an infinite and continuous distribution of sources, located beyond the infinite boundary S_∞ of the half-space, (dashed line in Fig. 1.1). For a review of the definition of a plane wave, the reader is referred to Aki & Richards (2002). As a result of the interactions between the incident wave and the body V_1, an scattered motion $u_j^S(\vec{x},\hat{i}\omega)$ is generated. This is an outgoing field that must damp out geometrically, reaching a vanishing limiting value at the infinite boundary S_∞. The purpose of the analysis is to determine the total motions inside the scatterer $u_i^t(\vec{x},\hat{i}\omega)$ and the scattered motions $u_i^S(\vec{x},\hat{i}\bar{\omega})$ inside the half-space. It is convenient, for mathematical and engineering purposes, to express the total field inside the

half-space $u_i(\vec{x},\hat{i}\omega)$, as the superposition of a free field motion $u_i^0(\vec{x},\hat{i}\omega)$ and the scattered motions $u_i^S(\vec{x},\hat{i}\omega)$ like;

$$u_i(\vec{x},\hat{i}\omega) = u_i^0(\vec{x},\hat{i}\omega) + u_i^S(\vec{x},\hat{i}\omega) \quad \text{for } \vec{x} \in V_0. \tag{1.1}$$

and where the free field term $u_i^0(\vec{x},\hat{i}\omega)$, corresponds to the solution that would exist in the half-space in the absence of the scatterer. This field can be found after solving the BVP for a perfect half-space subject to the incident field $u_i^{in}(\vec{x},\hat{i}\omega)$ and leading to a field reflected at the free boundary S_F and denoted by $u_i^R(\vec{x},\hat{i}\omega)$ yielding;

$$u_i^0(\vec{x},\hat{i}\omega) = u_i^{in}(\vec{x},\hat{i}\omega) + u_i^R(\vec{x},\hat{i}\omega) \quad \text{for } \vec{x} \in V_0. \tag{1.2}$$

With the above definitions at hand, the reduced wave equation governing the total motions inside the scatterer can be written like;

$${}_1L_{ij}u_j^t(\vec{x},\hat{i}\omega) + \rho_1\omega^2 u_i^t(\vec{x},\hat{i}\omega) = 0 \quad \text{for } \vec{x} \in V_1 \tag{1.3}$$

with the BVP being completely by the boundary conditions along S_1

$$t_i^t(\hat{n},\vec{x},\hat{i}\omega) = 0 \quad \text{for } \vec{x} \in S_1 \tag{1.4}$$

and the coupling conditions along S given by

$$\begin{aligned} &{}^1u_i^t(\vec{x},\hat{i}\omega) = {}^0u_i^t(\vec{x},\hat{i}\omega) \\ &{}^1t_i^t(\hat{n},\vec{x},\hat{i}\omega) + {}^0t_i^t(\hat{n}^*,\vec{x},\hat{i}\omega) = 0 \quad \text{for } \vec{x} \in S. \end{aligned} \tag{1.5}$$

In the above, the differential operator ${}_kL_{ij}$ is the Navier operator from theory of elasticity for the domain V_k and defined like;

$${}_kL_{ij} = (\lambda_k + \mu_k)\,\delta_{pj}\frac{\partial^2}{\partial x_i \partial x_p} + \mu_k \frac{\partial^2}{\partial x_j \partial x_j}$$

which results after relating the Cauchy stress tensor σ_{ij} to the infinitesimal strains tensor ϵ_{ij} through the generalized Hook's law for an isotropic homogeneous medium and substituting the

result into the conservation equations for the linear momentum. For a detailed review of the theory of elasticity model the reader is referred to Love (2013).

Similarly, the reduced wave equation governing the scattered motions inside the half-space is written like

$$ {}_0L_{ij}u_j^S(\vec{x},\hat{i}\omega) + \rho_0\omega^2 u_i^S(\vec{x},\hat{i}\omega) = 0 \quad \text{for } \vec{x} \in V_0 \tag{1.6} $$

and complemented with boundary conditions

$$ t_i^S(\hat{n}^*,\vec{x},\hat{i}\omega) = 0 \quad \text{for } \vec{x} \in S_F \tag{1.7} $$

and radiation boundary conditions along S_∞

$$ \begin{aligned} &\lim_{r\to\infty} r\left[\frac{\partial u_i^S}{\partial r} - \hat{i}\kappa u_i^S\right] = 0 \\ &\lim_{r\to\infty} u_i^S(\vec{x},\hat{i}\omega) = 0 \quad \text{for } \vec{x} \in S_\infty. \end{aligned} \tag{1.8} $$

In (1.5) the displacements ${}^1u_i^t(\vec{x},\hat{i}\omega)$ and ${}^0u_i^t(\vec{x},\hat{i}\omega)$ and the tractions ${}^1t_i^t(\hat{n},\vec{x},\hat{i}\omega)$ and ${}^0t_i^t(\hat{n}^*,\vec{x},\hat{i}\omega)$ represent total displacements and tractions along the internal coupling boundary S obtained as limits approaching the boundary from the inside domain V_1 and from the outside domain V_0 respectively. Using the superposition for the total field in the half-space in terms of free-field and scattered motions (1.1) these coupling conditions can also be written like;

$$ \begin{aligned} &{}^1u_i^t(\vec{x},\hat{i}\omega) = {}^0u_i^S(\vec{x},\hat{i}\omega) + u_i^0(\vec{x},\hat{i}\omega) \\ &{}^1t_i^t(\hat{n},\vec{x},\hat{i}\omega) + {}^0t_i^S(\hat{n}^*,\vec{x},\hat{i}\omega) + t_i^0(\hat{n}^*,\vec{x},\hat{i}\omega) = 0 \quad \text{for } \vec{x} \in S. \end{aligned} \tag{1.9} $$

1.1.2 Integral Formulation of the Boundary Value Problem

The BVP governing the total motions inside the scatterer and half-space, can alternatively be formulated in the form of integral equations with the aid of the elastodynamics representation theorem Eringen & Şuhubi (1975), Aki & Richards (2002). The resulting integral equations give rise to discrete boundary element method (BEM) algorithms, Banerjee (1994). For completeness, we also describe this technique since the resulting algorithms are highly accurate in the case of infinite and semi-infinite domains. These BEM algorithms can be directly implemented into

commercial finite element codes following the steps reported in this work since our formulation is general.

In the presented integral representations, we consider formulations with a half-space and a full-space Green tensor (i.e.,Lamb and Stokes tensors respectively). The representation in terms of the half-space Green function–simultaneously satisfying radiation and free-surface boundary conditions–results in a BEM discretization involving only boundary elements along the coupling surface S (Fig. 1.1). In contrast, if one uses the full-space Green's function, the discretization of the half-space must be extended laterally beyond the coupling surface. In this section we introduce the general elastodynamics representation theorem and apply it to generate two alternative integral equations for the scattered motions in the half-space.

Representation theorem for the scattered field

Consider once again the total response in the half-space as the superposition of the free-field motion plus the scattered waves, see Pao & Varatharajulu (1976)

$$u_i(\vec{x},\hat{i}\omega) = u_i^0(\vec{x},\hat{i}\omega) + u_i^S(\vec{x},\hat{i}\omega) \tag{1.10}$$

and where the free field motion u_i^0 corresponds to the solution for the half-space in the absence of the scatterer. Let us consider as starting point for all the subsequent integral formulations, the exact elastodynamics representation theorem for the scattered motions at a point $\vec{\xi}$ over the half-space Pao & Varatharajulu (1976) in terms of full-space Green's tensors expressed by:

$$\begin{aligned} u_i^S(\vec{\xi},\hat{i}\omega) = &\int_S \left[G_{ij}(\vec{x},\hat{i}\omega;\vec{\xi})t_j^S(\vec{x},\hat{i}\omega;\hat{n}^*) - H_{ij}(\vec{x},\hat{i}\omega,\hat{n}^*;\vec{\xi})u_j^S(\vec{x},\hat{i}\omega)\right]\,\mathrm{d}S(\vec{x}) - \\ &\int_{S_F} H_{ij}(\vec{x},\hat{i}\omega,\hat{n}^*;\vec{\xi})u_j^S(\vec{x},\hat{i}\omega)\,\mathrm{d}S(\vec{x}) + \\ &\int_{S_D} \left[G_{ij}(\vec{x},\hat{i}\omega;\vec{\xi})t_j^S(\vec{x},\hat{i}\omega;\hat{n}^*) - H_{ij}(\vec{x},\hat{i}\omega,\hat{n}^*;\vec{\xi})u_j^S(\vec{x},\hat{i}\omega)\right]\,\mathrm{d}S(\vec{x}) \quad \text{for } \vec{\xi}\in V_0 \end{aligned} \tag{1.11}$$

where $G_{ij}(\vec{x},\hat{i}\omega;\vec{\xi})$ and $H_{ij}(\vec{x},\hat{i}\omega,\hat{n}^*;\vec{\xi})$ are the displacement and tractions Green's tensors respectively. The relevant surfaces and parts of the domain in this integral equation were already described in Fig. 1.1. The representation theorem in Eq.(1.11), yielding the scattered motions $u_i^S(\vec{\xi},\hat{i}\omega)$ inside the half-space is exact, even for finite surfaces S_F and S_D as long as the fields $u_j^S(\vec{x},\hat{i}\omega)$ and $t_j^S(\vec{x},\hat{i}\omega;\hat{n}^*)$ to be prescribed along S_D are the correct ones.

In the integral formulation of the problem, it is convenient to write the radiation boundary conditions at S_∞ like;

$$\lim_{\vec{r}\to\infty}\int_{S_\infty}\left[G_{ij}(\vec{x},\hat{i\omega};\vec{\xi})t_j^S(\vec{x},\hat{i\omega};\hat{n}^*)-H_{ij}(\vec{x},\hat{i\omega},\hat{n}^*;\vec{\xi})u_j^S(\vec{x},\hat{i\omega})\right]\,\mathrm{d}S(\vec{x})=0.$$

Boundary integral equation with a half-space Green tensor $G_{ij}^{HS}(\vec{x},\hat{i\omega};\vec{\xi})$

A first representation can be derived directly from Eq.(1.11) if the used Green's functions satisfy the free surface boundary condition. After using the integral representation for the radiation conditions, we arrive at the following representation theorem for the scattered motions in the half space;

$$\begin{aligned}u_i^S(\vec{\xi},\hat{i\omega})=&\int_S G_{ij}^{HS}(\vec{x},\hat{i\omega};\vec{\xi})t_j^S(\vec{x},\hat{i\omega};\hat{n}^*)\,\mathrm{d}S(\vec{x})-\\&\int_S H_{ij}^{HS}(\vec{x},\hat{i\omega},\hat{n}^*;\vec{\xi})u_j^S(\vec{x},\hat{i\omega})\,\mathrm{d}S(\vec{x})\quad\text{for }\vec{\xi}\in V_0\end{aligned}\tag{1.12}$$

and where $G_{ij}^{HS}(\vec{x},\hat{i\omega};\vec{\xi})$ and $H_{ij}^{HS}(\vec{x},\hat{i\omega},\hat{n}^*;\vec{\xi})$ are the displacement and tractions Green's tensors for a half-space. The resulting BEM algorithm would only involve the mesh along the coupling surface S as shown in Figure 1.2a. This approach may result computationally expensive since the free surface boundary condition is difficult to satisfy. A known algorithm to enforce the traction free condition is the discrete wavenumber boundary element method (DWBEM), Kawase (1988), Kim & Papageorgiou (1993).

Boundary integral equation with a full-space Green tensor $G_{ij}(\vec{x},\hat{i\omega};\vec{\xi})$ and exact radiation condition

If the radiation condition along S_∞ expressed in integral form is subsequently imposed in Eq.(1.11), we obtain the following exact representation for the scattered motions in the half-space:

$$\begin{aligned}u_i^S(\vec{\xi},\hat{i\omega})=&\int_S\left[G_{ij}(\vec{x},\hat{i\omega};\vec{\xi})t_j^S(\vec{x},\hat{i\omega};\hat{n}^*)-H_{ij}(\vec{x},\hat{i\omega},\hat{n}^*;\vec{\xi})u_j^S(\vec{x},\hat{i\omega})\right]\,\mathrm{d}S(\vec{x})-\\&\int_{S_F}H_{ij}(\vec{x},\hat{i\omega},\hat{n}^*;\vec{\xi})u_j^S(\vec{x},\hat{i\omega})\,\mathrm{d}S(\vec{x})\quad\text{for }\vec{\xi}\in V_0.\end{aligned}\tag{1.13}$$

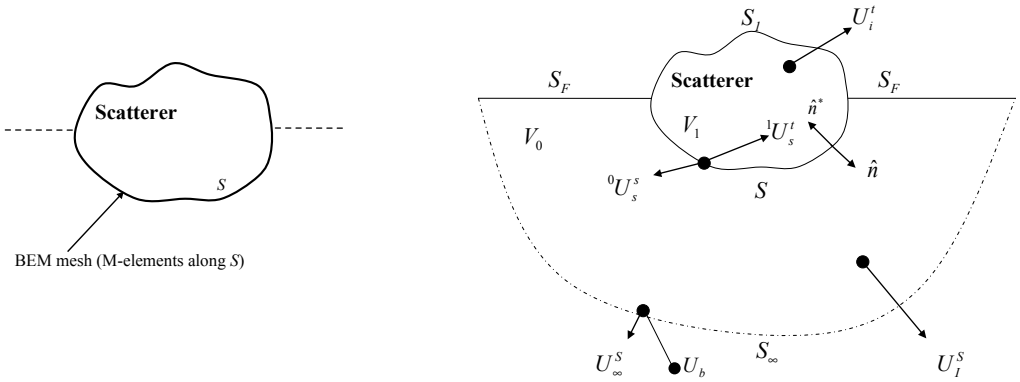

(a) **(b)**

Figure 1.2. Definition of the domain and the different instances appearing in the BEM schemes

Since the traction-free surface S_F has to be rendered finite in the computational model, it is only possible to satisfy Eq.(1.13) approximately as specified in Eq.(1.14) whereby we have used $\hat{S}_F$ to denote its finite extension

$$u_i^S(\vec{\xi},\hat{i}\omega) \approx \int_S \left[G_{ij}(\vec{x},\hat{i}\omega;\vec{\xi})t_j^S(\vec{x},\hat{i}\omega;\hat{n}^*) - H_{ij}(\vec{x},\hat{i}\omega,\hat{n}^*;\vec{\xi})u_j^S(\vec{x},\hat{i}\omega)\right] \mathrm{d}S(\vec{x}) - \int_{\hat{S}_F} H_{ij}(\vec{x},\hat{i}\omega,\hat{n}^*;\vec{\xi})u_j^S(\vec{x},\hat{i}\omega)\,\mathrm{d}S(\vec{x}) \quad \text{for } \vec{\xi} \in V_0. \tag{1.14}$$

Chapter 2

User Element Subroutine for Wave Propagation Analysis in the Frequency Domain

Introduction

In the particular case of commercial codes like ABAQUS or FEAP, the solution of a problem through user element subroutines, requires that the element contribution to the global coefficient matrix and excitations vector be provided. In this chapter we first describe the discrete form of a generalized scattering problem in wave propagation, as defined in Chapter 1 in terms of scattered motions. The shown matrix equations, are assembled by the code after receiving from the user the assembly information and the contribution from each element.

Although most of the problems treated in this work, correspond to mechanical waves propagating in classical elastic models, our description is general in the sense that no reference to a specific medium or kinematic assumption is made. For instance it can be easily modified to consider problems of plane strain or plane stress, three dimensional elasticity, antiplane waves, micropolar waves or even waves in other physical contexts. To maintain this generality we introduce the idea of generalized variables, e.g., generalized stress, strain and primary degrees of freedom. Since our formulation works in the frequency domain, we assume all these variables to be complex valued.

The finite element formulation follows classical ideas, starting from a generalized principle of virtual work. In order to cast our algorithm in real algebra, we double the number of degrees of freedom accounting for the real and imaginary part of each variable and perform the required products in the generalized variational statement. Finally, after using interpolation in the classical sense of the finite element method, we arrive at general equilibrium equations in the frequency

domain for a generalized medium, but written in terms of real variables. The equilibrium equations are written in terms of a generalized impedance matrix and a generalized loads vector. Since the formulation is equally valid for any domains, e.g., finite, full-space or half-space, we particularize the equations to the case of scattering by an object in a half-space, as is usual in earthquake engineering applications. We explicitly show the form of the elemental contributions depending on the part of the domain being occupied by the element.

In order to test the formulation we solve a simple, plane strain elasticity problem. We first obtain the response using a commercial code. Next, we assume the material to have an artificial complex valued modulus, so the resulting problem must be solved via our user element subroutine. As a test we verify that our solution approaches the real, elasticity solution as the imaginary part of the complex modulus approaches a null value. As a second verification example, we compute the response of a semi-circular canyon under incident P waves. We obtain the spatial distribution over the canyon surface of the frequency domain transfer function and compare it with the results predicted by Wong (1982), Kawase & Aki (1990). This problem is revisited in depth in subsequent chapters.

2.1 Discrete Formulation of a Generalized Wave Scattering Problem

In what follows we describe in a very general form the discrete version of the wave scattering problem described in the previous Chapter. In particular we make emphasis on the so-called half-space-super-element (HSSE) approximating the semi-infinite space boundary condition. The used notation for the involved degrees of freedom is defined in Fig. 2.1.

In discrete terms the governing equations for the scatterer can be written like

$$\left[S_{SC}(\hat{i}\omega)\right]\left\{{}^1U_S^t\right\} = \left\{{}^1F_S^t(\hat{n})\right\} \tag{2.1}$$

where $S_{SC}(\hat{i}\omega)$ is the impedance or dynamic stiffness matrix for the scatterer, while ${}^1F_S^t(\hat{n})$ are the interaction forces induced by the supporting half-space. Equation (2.1) is written in terms of degrees of freedom along the coupling surface S. In that sense the terms ${}^1U_S^t$ and ${}^1F_S^t(\hat{n})$ refer to limiting values for total nodal displacements and interaction forces evaluated over S, but approaching the surface from the inside of V_1.

Similarly, the discrete equations for the supporting half-space, formulated here in terms of a half-space-super-element (HSSE) represent the plane wave excitation and radiation boundary conditions. The equations for the super-element, can be achieved through either one of the formu-

lations described in Chapter 1. These are written in compact notation in terms of an impedance matrix $G_{HS}(\hat{i\omega})$ and interaction surface forces ${}^0F_S^s(\hat{n}^*)$ for degrees of freedom over S like

$$\left[G_{HS}(\hat{i\bar{\omega}})\right]\left\{{}^0U_S^s\right\} = \left\{{}^0F_S^s(\hat{n}^*)\right\}. \tag{2.2}$$

Using the discrete version of the coupling (or jump conditions (1.9)) valid on S

$$\begin{aligned} {}^1U_s^t &= {}^0U_s^S + U_s^0 \\ {}^1F_s^t(\hat{n}) &+ {}^0F_s^S(\hat{n}^*) + F_s^0(\hat{n}^*) = 0. \end{aligned} \tag{2.3}$$

and substituting (2.3) into (2.1) and (2.2), leads to the following discrete equilibrium equations for the complete scatterer-half-space system

$$\left[S_{SC}(\hat{i\omega}) + G_{HS}(\hat{i\omega})\right]\left\{{}^1U_S^t\right\} = \left\{-F_s^0(\hat{n}^*) + G_{HS}(\hat{i\omega}) * U_s^0\right\}. \tag{2.4}$$

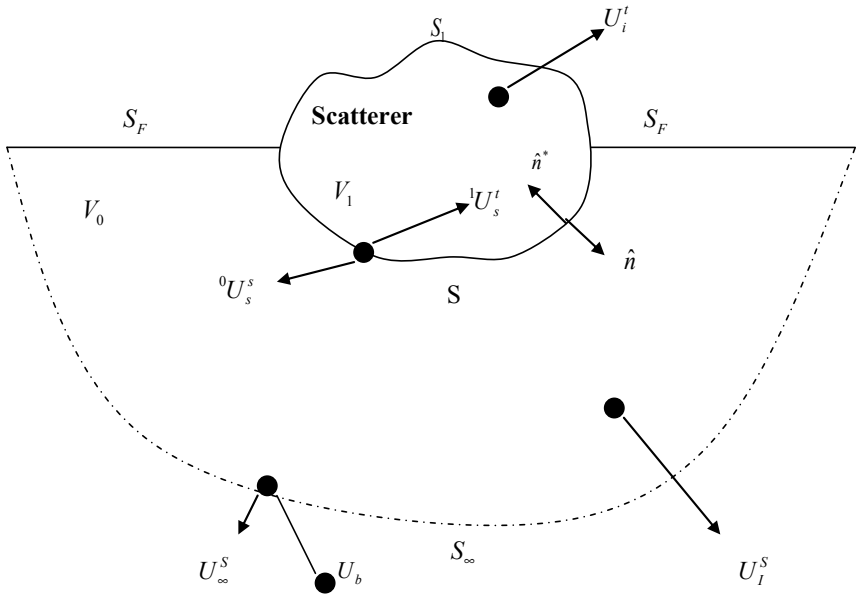

Figure 2.1. Definition of the degrees of freedom in a FEM discretization.

In (2.4) the loading term is composed of both, the incoming displacements U_s^0 and the consistent incoming nodal forces $F_s^0(\hat{n}^*)$. Once the impedance contribution $G_{HS}(\hat{i\omega})$ for the half-space is obtained, it can be coupled to any scatterer of impedance $S_{SC}(\hat{i\omega})$. This last contribution to global equilibrium, is regarded as a single finite element comprising the semi-infinite character

of the half-space, its radiation boundary conditions and the effective loads corresponding to the incoming field. We refer to this element as the Half-Space-Super-Element where;

$$\begin{aligned} S_{HSSE}(\hat{i}\omega) &\longleftarrow G_{HS})(\hat{i}\omega) \\ RHS_{HSSE} &\longleftarrow -F_S^0(\hat{n}^*) + G_{HS}(\hat{i}\omega) * U_s^0. \end{aligned} \tag{2.5}$$

In what follows we will derive a general formulation in real algebra of the frequency domain complex variables problem in terms of generalized impedance matrices like those stated in (2.4).

2.2 Finite element formulation in real algebra

Let Σ_{ij}, E_{ij} and ϕ_i be a generalized stress tensor, a generalized strain tensor and a generalized displacement vector and assume that the problem can be represented in terms of the following generalized principle of virtual work;

$$\int_V \Sigma_{ij}\delta E_{ij} dV - \hat{\rho}\omega^2 \int_V \phi_i \delta\phi_i dV - \int_S T_i \delta\phi_i dS = 0. \tag{2.6}$$

where the complex stress, strain and displacements are defined by;

$$\begin{aligned} \Sigma_{ij} &= \Sigma_{ij}^R + \hat{i}\Sigma_{ij}^I \\ E_{ij} &= E_{ij}^R + \hat{i}E_{ij}^I \\ \phi_i &= \phi_i^R + \hat{i}\phi_i^I \end{aligned} \tag{2.7}$$

and where T_i is a complex generalized projection of the stress tensor Σ_{ij} in the direction defined by the outward surface normal $\hat{n}$ and defined by $T_i = \Sigma_{ij}\hat{n}_i$.

Performing the products specified in (2.6) using (2.7) yields

$$
\begin{aligned}
\int_V \Sigma_{ij}\delta E_{ij} dV &= \int_V \Sigma_{ij}^R \delta E_{ij}^R dV - \int_V \Sigma_{ij}^I \delta E_{ij}^I dV - \\
&\hat{i}\left[\int_V \Sigma_{ij}^R \delta E_{ij}^R dV + \int_V \Sigma_{ij}^R \delta E_{ij}^R dV\right] \\
\int_V \phi_i \delta\phi_i dV &= \int_V \phi_i^R \delta\phi_i^R dV - \int_V \phi_i^I \delta\phi_i^I dV - \\
&\hat{i}\left[\int_V \phi_i^R \delta\phi_i^I dV + \int_V \phi_i^I \delta\phi_i^R dV\right] \\
\int_S T_i \delta\phi_i dS &= \int_S T_i^R \delta\phi_i^R dS - \int_S T_i^I \delta\phi_i^I dS - \\
&\hat{i}\left[\int_V T_i^R \delta\phi_i^I dS + \int_V T_i^I \delta\phi_i^R dS\right]
\end{aligned}
\tag{2.8}
$$

and substitution of (2.8) in (2.6) after separation of real and imaginary components results in the following real algebra PVW statements;

$$
\begin{aligned}
&\int_V \Sigma_{ij}^R \delta E_{ij}^R dV - \int_V \Sigma_{ij}^I \delta E_{ij}^I dV - \hat{\rho}\omega^2 \int_V \phi_i^R \delta\phi_i^R dV + \hat{\rho}\omega^2 \int_V \phi_i^I \delta\phi_i^I dV = \\
&\qquad \int_S T_i^R \delta\phi_i^R dS - \int_S T_i^I \delta\phi_i^I dS = 0 \\
&\int_V \Sigma_{ij}^R \delta E_{ij}^I dV - \int_V \Sigma_{ij}^I \delta E_{ij}^R dV - \hat{\rho}\omega^2 \int_V \phi_i^R \delta\phi_i^I dV + \hat{\rho}\omega^2 \int_V \phi_i^I \delta\phi_i^R dV = \\
&\qquad \int_S T_i^R \delta\phi_i^I dS + \int_S T_i^I \delta\phi_i^R dS = 0.
\end{aligned}
\tag{2.9}
$$

Introducing also a generalized constitutive tensor M_{ijkl} (where the tensor M_{ijkl} has imaginary components different from zero only when damping is considered) we can write

$$
\Sigma_{ij} = M_{ijkl} E_{kl}. \tag{2.10}
$$

In matrix form we have;

$$M = \begin{bmatrix} M^R_{ijkl} & -M^I_{ijkl} \\ M^I_{ijkl} & M^R_{ijkl} \end{bmatrix}$$

Using (2.7) and once again separating real and imaginary parts we have the following real constitutive relationships;

$$\begin{aligned} \Sigma^R_{ij} &= M^R_{ijkl} E^R_{kl} - M^I_{ijkl} E^I_{kl} \\ \Sigma^I_{ij} &= M^I_{ijkl} E^R_{kl} + M^R_{ijkl} E^I_{kl}. \end{aligned} \tag{2.11}$$

Discretization of each independent component of the generalized degrees of freedom, with standard shape functions N^K_i and where $\hat{\phi}^K_R$ and $\hat{\phi}^K_I$ represent nodal values corresponding to the real and imaginary displacements at the K^{th}-node allows us to write;

$$\begin{aligned} \phi^R_i &= N^K_i \hat{\Phi}^K_R \\ \phi^I_i &= N^K_i \hat{\Phi}^K_I. \end{aligned} \tag{2.12}$$

Similarly we can write for the strain components

$$\begin{aligned} E^R_{ij} &= B^K_{ij} \hat{\Phi}^K_R \\ E^I_{ij} &= B^K_{ij} \hat{\Phi}^K_I \end{aligned} \tag{2.13}$$

Using (2.11)-(2.13) in (2.9) results in the following discrete versions of the generalized principle of virtual work;

$$\begin{aligned} &\delta\hat{\Phi}^K_R \int_V B^K_{ij} M^R_{ijkl} B^P_{kl} dV \hat{\Phi}^P_R - \delta\hat{\Phi}^K_R \int_V B^K_{ij} M^I_{ijkl} B^P_{kl} dV \hat{\Phi}^P_I - \\ &\delta\hat{\Phi}^K_I \int_V B^K_{ij} M^I_{ijkl} B^P_{kl} dV \hat{\Phi}^P_R - \delta\hat{\Phi}^K_I \int_V B^K_{ij} M^R_{ijkl} B^P_{kl} dV \hat{\Phi}^P_I - \\ &\hat{\rho}\omega^2 \delta\hat{\Phi}^K_R \int_V N^K_i N^P_i dV \hat{\Phi}^P_R + \hat{\rho}\omega^2 \delta\hat{\Phi}^K_I \int_V N^K_i N^P_i dV \hat{\Phi}^P_I = \\ &\qquad \delta\hat{\Phi}^K_R \int_S N^K_i t^R_i dS - \delta\hat{\Phi}^K_I \int_S N^K_i T^I_i dS \end{aligned} \tag{2.14}$$

$$\begin{aligned}
&\delta\hat{\Phi}_I^K \int_V B_{ij}^K M_{ijkl}^R B_{kl}^P dV \hat{\Phi}_R^P - \delta\hat{\Phi}_I^K \int_V B_{ij}^K M_{ijkl}^I B_{kl}^P dV \hat{\Phi}_I^P - \\
&\delta\hat{\Phi}_R^K \int_V B_{ij}^K M_{ijkl}^I B_{kl}^P dV \hat{\Phi}_R^P - \delta\hat{\Phi}_R^K \int_V B_{ij}^K M_{ijkl}^R B_{kl}^P dV \hat{\Phi}_I^P - \\
&\hat{\rho}\omega^2 \delta\hat{\Phi}_I^K \int_V N_i^K N_i^P dV \hat{\Phi}_R^P + \hat{\rho}\omega^2 \delta\hat{\Phi}_R^K \int_V N_i^K N_i^P dV \hat{\Phi}_I^P = \\
&\qquad\qquad \delta\hat{\Phi}_I^K \int_S N_i^K t_i^R dS + \delta\hat{\Phi}_R^K \int_S N_i^K T_i^I dS
\end{aligned} \tag{2.15}$$

From the arbitrary condition of $\delta\hat{\Phi}_R^K$ and $\delta\hat{\Phi}_I^K$ in (2.14) and (2.15) we have the following equivalent system of real equations in the unknown generalized nodal displacements $\hat{\Phi}_R^P$ and $\hat{\Phi}_I^P$;

$$\begin{aligned}
&\int_V B_{ij}^K M_{ijkl}^R B_{kl}^P dV \hat{\Phi}_R^P - \int_V B_{ij}^K M_{ijkl}^I B_{kl}^P dV \hat{\Phi}_I^P - \\
&\qquad \hat{\rho}\omega^2 \int_V N_i^K N_i^P dV \hat{\Phi}_R^P = \int_S N_i^K T_i^R dS \\
&- \int_V B_{ij}^K M_{ijkl}^I B_{kl}^P dV \hat{\Phi}_R^P - \int_V B_{ij}^K M_{ijkl}^R B_{kl}^P dV \hat{\Phi}_I^P + \\
&\qquad \hat{\rho}\omega^2 \int_V N_i^K N_i^P dV \hat{\Phi}_I^P = -\int_S N_i^K T_i^I dS
\end{aligned} \tag{2.16}$$

and

$$\begin{aligned}
&\int_V B_{ij}^K M_{ijkl}^R B_{kl}^P dV \hat{\Phi}_R^P - \int_V B_{ij}^K M_{ijkl}^I B_{kl}^P dV \hat{\Phi}_I^P - \\
&\qquad \hat{\rho}\omega^2 \int_V N_i^K N_i^P dV \hat{\Phi}_R^P = \int_S N_i^K T_i^R dS \\
&\int_V B_{ij}^K M_{ijkl}^I B_{kl}^P dV \hat{\Phi}_R^P + \int_V B_{ij}^K M_{ijkl}^R B_{kl}^P dV \hat{\Phi}_I^P - \\
&\qquad \hat{\rho}\omega^2 \int_V N_i^K N_i^P dV \hat{\Phi}_I^P = \int_S N_i^K T_i^I dS
\end{aligned} \tag{2.17}$$

which can be written in matrix form like

$$\begin{bmatrix} \int\limits_V B_{ij}^K M_{ijkl}^R B_{kl}^P dV & -\int\limits_V B_{ij}^K M_{ijkl}^I B_{kl}^P dV \\ \int\limits_V B_{ij}^K M_{ijkl}^I B_{kl}^P dV & \int\limits_V B_{ij}^K M_{ijkl}^R B_{kl}^P dV \end{bmatrix} \begin{Bmatrix} \hat{\Phi}_R^P \\ \hat{\Phi}_I^P \end{Bmatrix} - \hat{\rho}\omega^2 \begin{bmatrix} \int\limits_V N_i^K N_i^P dV & 0 \\ 0 & \int\limits_V N_i^K N_i^P dV \end{bmatrix} \begin{Bmatrix} \hat{\Phi}_R^P \\ \hat{\Phi}_I^P \end{Bmatrix} = \begin{Bmatrix} \int\limits_S N_i^K T_i^R dS \\ \int\limits_S N_i^K T_i^I dS \end{Bmatrix} . \tag{2.18}$$

Since the stiffness term in (2.18) is anti-symmetric we actually solve the system for the modified degrees of freedom $\bar{\hat{\Phi}}_I^P = -\hat{\Phi}_I^P$ with the corresponding sign change in the impedance matrix terms so symmetry is restored.

In the actual implementation, within the context of the user element subroutines in a commercial finite element code, each element contributes with a coefficient matrix $S(\hat{i}\omega)$ given by;

$$S(\hat{i}\omega) = \begin{bmatrix} \int\limits_V B_{ij}^K M_{ijkl}^R B_{kl}^P dV & -\int\limits_V B_{ij}^K M_{ijkl}^I B_{kl}^P dV \\ \int\limits_V B_{ij}^K M_{ijkl}^I B_{kl}^P dV & \int\limits_V B_{ij}^K M_{ijkl}^R B_{kl}^P dV \end{bmatrix} - \hat{\rho}\omega^2 \begin{bmatrix} \int\limits_V N_i^K N_i^P dV & 0 \\ 0 & \int\limits_V N_i^K N_i^P dV \end{bmatrix} \tag{2.19}$$

and with a right-hand-side vector $RHS(\hat{i}\omega)$ of the general form;

$$RHS(\hat{i}\omega) = \begin{Bmatrix} \int\limits_S N_i^K T_i^R dS \\ \int\limits_S N_i^K T_i^I dS \end{Bmatrix} . \tag{2.20}$$

2.3 Scattering of plane waves

The problem domain and the corresponding degrees of freedom in each relevant region are once again described for completeness in Fig. 3.1. The full domain is divided into; the scatterer V_1

bounded by the free surface S_1 and the internal surface S; the half-space V_0 bounded by the free surface S_F, the internal surface S and the conceptual surface at infinity S_∞. Notice that the internal surface S couples the scatterer to the half-space subdomain. In a finite element representation of the half-space, the conceptual surface S_∞ must be approximated by a finite artificial truncation surface S_D over which absorbing boundaries trying to mimic the radiation condition on S_∞ are specified.

We now specify the independent contributions from the elements located in each individual part of the domain after using the following definitions for the generalized degrees of freedom: Φ_i=degrees of freedom in the interior of the scatterer and along the free surface S_1, Φ_S=degrees of freedom along the coupling surface S, Φ_I=degrees of freedom over the half-space and its boundary (excluding S). Similarly,the impedance matrices are defined like $S^1(\hat{i\omega})$=impedance matrix for the scatterer, $S^0(\hat{i\omega})$=impedance matrix for the half-space and $S^D(\hat{i\omega})$=impedance matrix for the absorbing boundaries (and with a similar notation applying for the right hand side vectors).

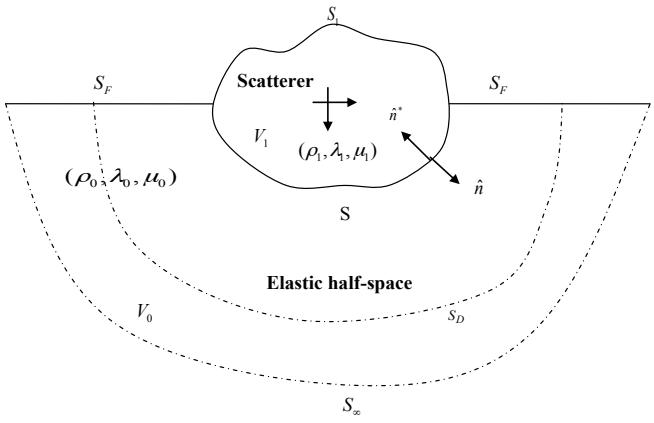

Figure 2.2. Definition of the problem domain.

In the actual implementation in a commercial software, we specified the following elemental coefficient matrices $S(\hat{i\omega})$ and right hand side vectors $RHS(\hat{i\omega})$ through user element subroutines.

Scatterer Elements

Accordingly, we define the contribution from the scatterer elements to the global discrete equilibrium equations by the terms

$$S^1(\hat{i\omega}) = \begin{bmatrix} S^1_{ii} & S^1_{iS} \\ S^1_{Si} & S^1_{SS} \end{bmatrix} \quad R\hat{H}S^1(\hat{i\omega}) = \begin{Bmatrix} 0 \\ 0 \end{Bmatrix}. \tag{2.21}$$

Strip Elements

Similarly, the contribution from the elements located in the half-space but in direct contact with the scatterer is given by the terms

$$S^0(\hat{i}\omega) = \begin{bmatrix} S^0_{SS} & S^0_{SI} \\ S^0_{IS} & S^0_{II} \end{bmatrix} \quad R\hat{H}S^0(\hat{i}\omega) = \begin{Bmatrix} -S^0_{SI}\Phi^0_I \\ S^0_{IS}\Phi^0_S \end{Bmatrix} \tag{2.22}$$

and where Φ^0_S and Φ^0_I represent the displacement from the incoming field evaluated at the nodal points along the coupling surface S and along an internal surface S_I separated 1 element width from S. This formulation corresponds to an application to the case of plane waves of the so-called domain reduction method (DRM) proposed by Bielak et al. (2003) in the context of localized point sources.

Absorbing Boundaries

Over the finite boundary S_D representing an approximation of the infinite surface S_∞, the contribution of the absorbing boundaries reduces to the specification of a complex spring with impedance $\hat{K}$. In the appendix we show the specific details of the implementation of absorbing boundaries for an in-plane problem in a classical medium.

Global System

After assembling the different elements through the model the final global system of equations reads;

$$\begin{bmatrix} S^1_{ii} & S^1_{iS} & 0 & 0 \\ S^1_{Si} & S^1_{SS} + S^0_{SS} & S^0_{SI} & 0 \\ 0 & S^0_{IS} & S^0_{II} & 0 \\ 0 & 0 & 0 & K \end{bmatrix} \begin{Bmatrix} \Phi_i \\ \Phi_S \\ \Phi^S_I \\ \Phi^S_D \end{Bmatrix} = \begin{Bmatrix} 0 \\ -S^0_{SI}\Phi^0_I \\ S^0_{IS}\Phi^0_S \\ 0 \end{Bmatrix} \tag{2.23}$$

where it must be noticed that over the half-space the problem is formulated in terms of the scattered motions Φ^S_I only.

2.4 Verification Problems

2.4.1 Simple Elasticity Problem

In order to test the implementation the simple 2D plane strain static elasticity problem shown in Figure 2.3 was considered. It consisted of a simple assemblage of second order quadratic elements submitted to normal and tangential stresses. The problem was first solved with standard, displacement based finite elements available in ABAQUS and then with the user element subroutine. An artificious damping coefficient ξ was used to introduced the imaginary components. A null value of this damping parameter recovers the classical solution. The problem was additionally solved manually.

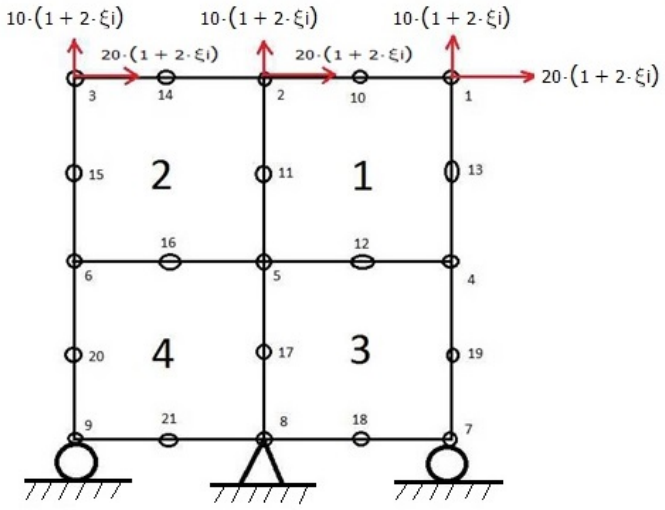

Figure 2.3. Assemblage for static validation of the implemented user element subroutine.

In the case of a classical elastic material the generalized stress and strain tensors $\Sigma_{ij} = (\sigma^R_{ij}, \sigma^I_{ij})$ and $E_{ij} = (\epsilon^R_{ij}, \epsilon^I_{ij})$ are related through the generalized constitutive tensor M_{ijkl} defined as follows for a plane strain problem

$$\hat{M} = \begin{bmatrix} \lambda+2\mu & \lambda & 0 & \hat{\lambda}+2\hat{\mu} & \hat{\lambda} & 0 \\ \lambda & \lambda+2\mu & 0 & \hat{\lambda} & \hat{\lambda}+2\hat{\mu} & 0 \\ 0 & 0 & \mu & 0 & 0 & \hat{\mu} \\ \hat{\lambda}+2\hat{\mu} & \hat{\lambda} & 0 & -(\lambda+2\mu) & -\lambda & 0 \\ \hat{\lambda} & \hat{\lambda}+2\hat{\mu} & 0 & -\lambda & -(\lambda+2\mu) & 0 \\ 0 & 0 & \hat{\mu} & 0 & 0 & -\mu \end{bmatrix} \tag{2.24}$$

and where $\hat{\lambda} = 2\xi\hat{i}\lambda$, $\hat{\mu} = 2\xi\hat{i}\mu$, λ and μ are the Lamé constants from theory of elasticity, σ_{ij} is the Cauchy stress tensor and ϵ_{ij} is the infinitesimal strains tensor.

The following set of complex loading was applied in the normal and tangential direction;

$$\begin{aligned} P_x &= 20(1+2\xi\hat{i}) \\ P_y &= 10(1+2\xi\hat{i}) \end{aligned} \tag{2.25}$$

with $\xi = 0.8$, $\hat{\nu} = 0.3(1.0+2\xi\hat{i})$, $\hat{E} = 210.000(1.0+2\xi\hat{i})$. We solved the problem manually, with the implemented user element subroutine as initial validation and with classical real elements using $\xi = 0$. The results from the manual solution and those obtained with the ABAQUS user subroutine are reported in Figure 2.4 and 2.5.

uR =

1	0.00393578651088299
2	0.00371666799869336
3	0.00417169422909165
4	0.00186935591999091
5	0.00182535636335764
6	0.00183930984718861
7	0.00110023309056272
8	0
9	0.00120565440882958
10	0.0037800946719862
11	0.0028222351252681
12	0.00181756350291542
13	0.00283930099337698
14	0.00389536620157263
15	0.00283590411640301
16	0.00180234393977678
17	0.00108171735746243
18	0.00064241829665056
19	0.0009586810174442
20	0.00096016867170048
21	0.00068574239944

vR =

1	-0.00139512887308985
2	0.00020406790997263
3	0.00212795451845384
4	-0.0013582263899271
5	0.00012429170740324
6	0.00164316798036898
7	0
8	0
9	0
10	-0.00056218131250896
11	0.00016673054978939
12	-0.00047157240232492
13	-0.00143124983120709
14	0.00092812890682681
15	0.00192425800578054
16	0.00074306812237356
17	0.00007157999071943
18	-0.00054441769151693
19	-0.00078099438351515
20	0.00090958574985241
21	0.00070686279501932

uI =

1	0.00032714245321135
2	0.00028941780829617
3	0.0002678573144259
4	0.00002880254930232
5	0.00017358220879394
6	-0.00010646530556409
7	0.00011483255402953
8	0
9	0.00001584175016246
10	0.00026376515634328
11	0.00021185251869656
12	0.00016167214174675
13	0.00023780255940929
14	0.00026723776914495
15	0.00012536974933209
16	0.00011098723101236
17	0.00011173422181287
18	0.00024840787383193
19	-0.00003774444613844
20	-0.00014725158010776
21	0.00018661150334495

vI =

1	-0.00014937069932642
2	-0.00000086346198049
3	0.00023625626876491
4	-0.00031644035561756
5	0.00001237079102199
6	0.00033002190590041
7	0
8	0
9	0
10	-0.00009974283640987
11	0.00001808564793262
12	-0.00009432230489915
13	-0.00028371236111073
14	0.00016335443832307
15	0.0003541208863705
16	0.00011726817741313
17	0.00000487305531479
18	-0.00011007617631944
19	-0.00006778283367357
20	0.00005437655724128
21	0.00007154886817347

Figure 2.4. Nodal displacements corresponding to the manual solution.

Node Label	u.Magnitude	u_real	v_real	u_imag	v_imag
1	4.18853434E-03	3.93578596E-03	-1.39512867E-03	327.142363E-06	-149.370680E-06
2	3.73350014E-03	3.71666742E-03	204.067881E-06	289.417745E-06	-863.455966E-09
3	4.69073188E-03	4.17169370E-03	2.12795427E-03	267.857220E-06	236.256252E-06
4	2.31086533E-03	1.86935568E-03	-1.35822617E-03	28.8025240E-06	-316.440302E-06
5	1.83779886E-03	1.82535616E-03	124.291691E-06	173.582172E-06	12.3707923E-06
6	2.46868283E-03	1.83930958E-03	1.64316769E-03	-106.465319E-06	330.021867E-06
7	1.10620935E-03	1.10023294E-03	-53.8849480E-36	114.832525E-06	-85.8699886E-36
8	0.	59.9999982E-36	17.7698916E-36	96.0000006E-36	27.7399763E-36
9	1.20575831E-03	1.20565423E-03	66.1150541E-36	15.8417261E-06	106.130013E-36
10	3.83076118E-03	3.78009421E-03	-562.181231E-06	263.765076E-06	-99.7428215E-06
11	2.83508189E-03	2.82223476E-03	166.730533E-06	211.852457E-06	18.0856496E-06
12	1.88468955E-03	1.81756320E-03	-471.572333E-06	161.672098E-06	-94.3222913E-06
13	3.18851881E-03	2.83930055E-03	-1.43124966E-03	237.802495E-06	-283.712317E-06
14	4.01331671E-03	3.89536563E-03	928.128778E-06	267.237687E-06	163.354416E-06
15	3.42940749E-03	2.83590378E-03	1.92425773E-03	125.369697E-06	354.120828E-06
16	1.95266772E-03	1.80234364E-03	743.067998E-06	110.987196E-06	117.268166E-06
17	1.08982576E-03	1.08171720E-03	71.5799833E-06	111.734204E-06	4.87305624E-06
18	877.951039E-06	642.418163E-06	-544.417591E-06	248.407829E-06	-110.076158E-06
19	1.23705191E-03	958.680874E-06	-780.899310E-06	-37.7444594E-06	-67.7832722E-06
20	1.33077148E-03	960.168545E-06	909.585622E-06	-147.251587E-06	54.3765527E-06
21	1.00235781E-03	685.742300E-06	706.862658E-06	186.611462E-06	71.5488568E-06

Figure 2.5. Nodal displacements corresponding to the UEL solution.

On the other hand, the results obtained with a null value of the artificial damping parameter are exactly equivalent to the ones obtained with standard elements available in ABAQUS.

2.4.2 Scattering of Plane P waves by a Cylindrical Canyon in a Half-Space

As a second verification example but now applied to a wave propagation problem, we solved the scattering of a P wave incident against a cylindrical canyon in a half-space. This problem has been previously solved by Kawase (1988) in the context of topographic effects in earthquake engineering, using a boundary integral equation formulation with half-space Green's functions represented in the wave number domain. The problem has become a benchmark solution to validate numerical methods and to develop fundamental understanding of topographic effects in earthquake engineering. The geometry of the problem is shown in Figure 2.6. The characteristic dimension of the canyon corresponds to a radius $a = 1.0\,Km$. The mechanical properties of the half-space correspond to $\rho = 1\,kg/m^3$, $\beta = 1\,km/s$ and a Poissons ratio $\nu = 1/3$. The excitation consisted of a Ricker pulse of central frequency $fc = 1.0\,Hz$, maximum frequency $fmax = 4.0\,Hz$ and time duration $Tmax = 8.0\,s$ applied at incidence angles (with respect to the vertical) corresponding to 0^o and 30^o . The analysis in the frequency domain was conducted with a frequency step of $\Delta f = fmax/32$. For the meshes were used 8-noded quadratic elements with characteristic dimensions satisfying the $\lambda_c/10$ criteria, where λ_c is the characteristic wavelength to be propagated (see Figure 2.6). In the analyses, absorbing boundaries were located at $1.0Km$ from the bottom of the canyon. For this validation the spatial distribution of the transfer function along the canyon surface is shown and compared with the solution computed with the in-house software DAMIAN in Figure 2.7. This problem will be revisited in greater detail in the next section.

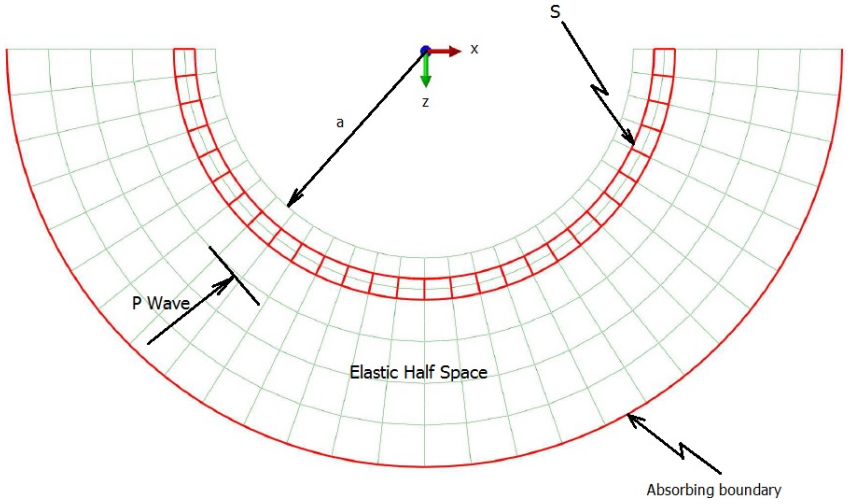

Figure 2.6. Finite element mesh for the semi-circular canyon.

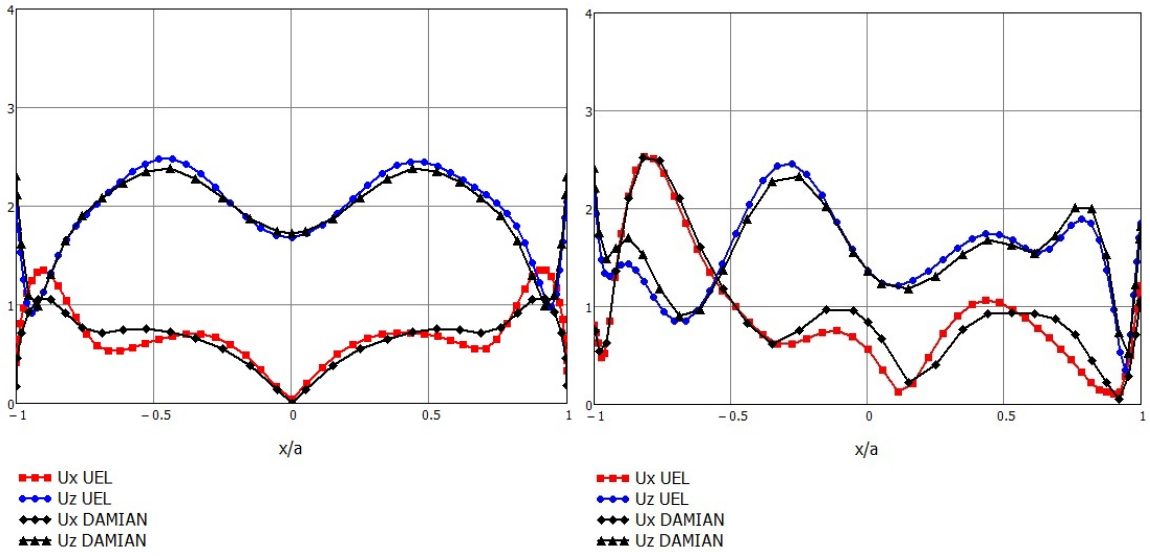

Figure 2.7. Spatial distribution for the frequency domain transfer function over the canyon surface for a dimensionless frequency $\eta = 1.0$. The function corresponds to the amplitude of the Fourier spectral response normalized over the amplitude of the incident wave. The function on the left corresponds to vertical incident and the one in the right to 30.0^0 incidence.

Chapter 3

The Problem of Site Effects in Earthquake Engineering

Introduction

The frequency and spatial variations introduced by local topography on seismic ground motions are known to produce concentrated damage during earthquakes (e.g.,Northridge, California-1994; Kobe, Japan-1997; Kocaeli, Turkey-1999). In the theory of elastodynamics the quantification of these effects implies the solution of a wave scattering problem. Modern numerical techniques and the available computer power, has led to the possibility of realistic simulations of these effects for large scale regional domains, e.g.,(Bao et al., 1998; Okamoto et al., 2011; Taborda & Bielak, 2011; Cupillard et al., 2012; Restrepo et al., 2012). At the same time, actual field records of large urban areas have become increasingly available during the last years providing additional evidence of the effects of topography. Despite these strong advances on the field, a detailed understanding of the underlying physics of the problem is still required.

In this chapter we address the problem of site effects in earthquake engineering from two point of views. In the first section of the chapter, we focus on the role played by the diffracted part of the motion on the modification induced by surface topographies. This idea is motivated by the fact, that in other problems related to propagation of acoustic and/or electromagnetic waves, the diffraction field has been clearly associated to the interaction of waves with geometric singularities. In earthquake engineering that idea has not been explored so far. In this work we use the numerical solution corresponding to the complete field and with the aid of the geometrical theory of raids we isolate the diffracted part of the motion. In particular we try to answer the question whether or not this part of the response capture the modifications induced by the site effects problem.

The second problem, related to the study of site effects, deals with the question of regional

versus truly local effects. In particular, we try to answer the question of how important are the regional effects in the local response a given site. In order to explore an analysis approach to this problem we use a simple model of a canyon with the shape of a circular sector containing two localized regions with different material properties. We use our user element subroutines to address both problems where the frequency domain response is highly relevant. As analysis tool we proceed in a two-step algorithm taking as a starting point a method proposed by Professor's Bielak group at Carnegie Mellon University originally formulated to save computer resources maintaining accuracy in the computations. That method has been called by its authors the domain reduction method as will be described later. In this work, since a different use is being made of the method we called it the modified domain reduction method.

3.1 The role of diffraction in the site effects problem

In this section we study the effects of topography on seismic ground motions, using a partition of the field into physically meaningful terms based upon the concept of diffracted motions. In earthquake engineering the terms scattering and diffraction have been used loosely as synonyms, Sanchez-Sesma & Iturraran-Viveros (2001), Mow & Pao (1971), however they are not. A strict definition of scattered field has been first attributed to Rayleigh: "A scattered wave is the difference of the total wave field observed in the presence of an obstacle and the incident wave". In the case of an obstacle being in a half-space, it is the difference of the total wave and the free field, Pao & Varatharajulu (1976). On the other hand, according to Keller (1962), diffracted waves are produced by incident waves which hit edges, corners or vertices of boundary surfaces or which graze such surfaces. This connection between the diffracted field and the geometric entities in the scatterer is expected to be reflected in the topographic effects.

The theory of diffraction has a long history. Its physical aspects have been studied in great detail, mainly in the context of electromagnetic waves. A landmark contribution and converted thereby in one of the building blocks for advancing the theory, is identified in the work of Sommerfeld (1896). He found the complete solution for the diffraction of electromagnetic plane waves by a semi-infinite crack in a homogeneous medium. Shortly after Sommerfeld's work, MacDonald (1902) delivered the solution for the total field on a wedge, under plane and cylindrical SH waves. He wrote the total field as series expansions in terms of Bessel functions. A detailed study of Macdonald's solution, highlighting various aspects of the diffracted field can be found in Sanchez-Sesma (1985).

A major push to the theory was also imparted by Keller (Keller, 1956, 1957), who conducted studies on the diffraction of electromagnetic waves by a convex cylinder and and aperture. Later Keller (1962), initiated the development of the now well recognized geometrical theory of diffraction (GTD). In one of his mains contributions he studied the canonical problem of a generalized wedge composed of an edge enclosed by a convex or a concave surface. The most salient feature of the

GTD is the introduction of diffraction coefficients, which upon application on the incident rays hitting the geometric singularity would deliver diffracted rays (e.g., just like reflection coefficients are used upon the incident field in a half-space). The diffraction coefficients in Keller's work failed on the transition regions adjacent to shadow and reflection boundaries. This was later improved by Kouyoumjian & Pathak (1974) who completed Keller's GTD producing a workable expression to predict the diffraction by a generalized wedge.

Within the specific context of earthquake engineering, the particular contribution from the diffracted field to the total solution has not received much attention. In that area the problem has been traditionally solved in terms of the scattered field. A possible explanation may be due to practical reasons for both engineers and mathematicians and also, because of the lack of a sound theory of diffraction of mechanical waves. A particular reference to the role played by the diffracted field in the site effects problem can be found in the work of Sanchez-Sesma and its co-workers. For example in Sanchez-Sesma (1985) the author revisited Macdonald's solution directly in the frequency domain. It was pointed out the fact that large differential motions were introduced by the diffracted field in the presence of shadow zones.

A partition of the field into incident, reflected and diffracted waves is also explicitly displayed by Sánchez-Sesma & Iturrarán-Viveros (2001) in the study of diffraction of plane SH waves by a finite crack in a full space. They obtained a near field solution by superposition of two semi-infinite cracks of the Sommerfeld type. These authors explicitly isolated the diffracted field. Later Iturrarán-Viveros et al. (2010) followed the same technique to find the solution for the diffraction by a cylindrical wave.

In contrast to the antiplane problem, in the case of in-plane waves the analytical solutions related to the diffracted field are just a few and the problem has been studied mainly from the numerical point of view. In this case complexities arise because of the coupling of boundary conditions and mode conversions at interfaces. One of the few particular solutions directly addressing diffraction is the one due to Achenbach (1973), who treated the problem of a semi-infinite slit under longitudinal waves obtained via integral transforms together with the Wiener-Hopf technique and the Cagniard-de-Hoop method. In the slit problem, the total field was shown to be composed of the incident P wave, reflected and diffracted P and SV waves and head waves connecting the diffracted P and SV fronts.

In a recent contribution Jaramillo et al. (2013), using the solution from Kouyoumjian & Pathak (1974) as a building block, proposed a superposition based diffraction technique (SBD), to study site effects due to topographic formations of arbitrary shape. In that method the surface topography is partitioned into several generalized wedges, each one of which contributes with a primary source of diffraction to the total field. Although the resulting method is cumbersome to apply if one wishes to find the complete solution everywhere, it is a useful tool that can be used in the interpretation of results from complex scenarios. It is in that study where we find the motivation for this work.

In our treatment of topographic effects we obtain the diffracted field from the complete solution computed numerically. Our interest lies in establishing a connection between the topographic effect and the diffracted motions. For that purpose we study the two simple problems of cylindrical canyons of semi-circular and rectangular cross sectional shapes. Those two problems differ in the number of diffraction sources. Although from the very concept of diffraction it is clear that it is related to a geometric effect, the idea has seldom been explored in order to study the effect of topography on earthquake induced ground motions. The physically based partition provided by the diffracted field, is expected to reveal conceptual aspects of the response not evident in the traditional scattering approach. In this chapter we address the effects of topography on the incident ground motions using the diffracted field as a physical characterization of the site effects that directly links the geometry of the scatterer to the motion at a given receiver. The aim of this preliminary study is to contribute with the understanding of the topographic or site effects problem by proposing an alternative methodology to isolate the geometric effects and to suggest a partition of the field that can be used to isolate also the mechanical effects.

3.1.1 Prediction of the diffracted field

In the classical approach of the scattering problem, the solution is written as the contribution from the free field and the scattered motions, Pao & Varatharajulu (1976). However, while the free-field is well understood, the scattered motions are not. In problems involving arbitrary scattering surfaces, like canyons and ridges, an alternative physically sound way of studying the topographic effect is through the use of the concept of diffraction understood in the sense of optics. As described before, the diffracted motions correspond to that part of the response that cannot be predicted by geometrical methods. For example, if in a given problem the involved scattering surfaces are at least C^2-continuous and fully illuminated, a complete, continuous solution, can be constructed based on geometrical methods without formally solving the elastodynamics wave equation. However, if there are shadow zones or geometric singularities, the diffracted field is required in order to smooth out any discontinuities existing in the geometric field. Our proposed analysis method is based on this idea, where the total response is separated into the geometric and diffracted parts. In this way, a direct physical connection between the solution and the topographic features of the scatterer can be established in a source-receiver basis. In this section we describe these alternative partitions of the field and establish different relations between the involved terms. In particular we show how to obtain the diffracted field from the total displacement.

For the discussion that follows it is convenient to define the scattering problem with domain defined in Figure 3.1. It is composed of the homogeneous isotropic elastic-half space V_0 with a scatterer or topographic irregularity V_1. The half-space and scatterer are assumed to be perfectly coupled along the internal contact surface S. Similarly, S_F = traction-free surface of the half-space, S_∞ = external remote surface of the half-space where radiation conditions are prescribed: whenever S_∞ is rendered finite in a computational representation, this surface becomes the internal truncation surface S_D and S_F becomes a finite surface denoted thereby like $\hat{S}_F$. The whole system

is then subjected to incident harmonic plane waves with a time dependence $e^{\hat{i}\omega t}$ (which is omitted here an hereafter) and where ω = circular frequency and $\hat{i} = \sqrt{-1}$. The scatterer and half-space are mechanically defined by the following parameters: ρ_i = mass density, μ_i = shear modulus, λ_i = Lame constant and where i=1, and 0 for the scatterer and half-space respectively. The purpose of the analysis is to determine the motions in the scatterer and inside the half-space due to the incident wave.

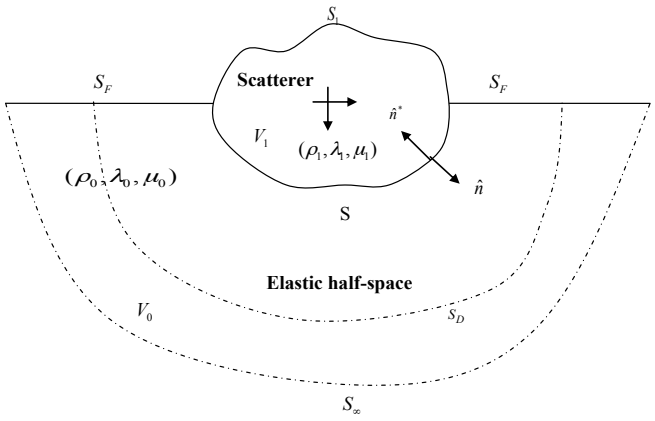

Figure 3.1. Definition of the problem domain.

In the classical formulation we write the total solution inside the half-space like;

$$u^T = u^{IN} + u_A^R + u^S \equiv u_A^0 + u^S \tag{3.1}$$

where u^{IN}=incident field, u_A^R=field reflected over the free surface of the half-space in the absence of the scatterer and the field defined from the superposition $u^{IN} + u_A^R \equiv u_A^0$ is the free field evaluated along the (fictitious) contact surface S. Due to its mathematical nature we also refer to this component of the total motion as the artificial incoming field. In (3.1), it is evident that the scattered contribution u^S, is the difference between the total motions and the artificial incoming field u_A^0. This construction process of the final complete solution is schematically represented in Figure 3.2.

Alternatively, the total solution could be written generalizing the concept of scattering as a relative displacement as we elaborate next. With the aid of Figure 3.3 in a first analysis step we solve the problem with the scatterer being removed but leaving the contact surface S as a free surface where the traction vanishes. The solution to this intermediate problem can be constructed superimposing the diffracted field u^D to the geometric solution $u_P^0 = u^{IN} + u_P^R$ where u_P^R=physical reflection of the incident rays over the common interface S. The resulting partition is written like;

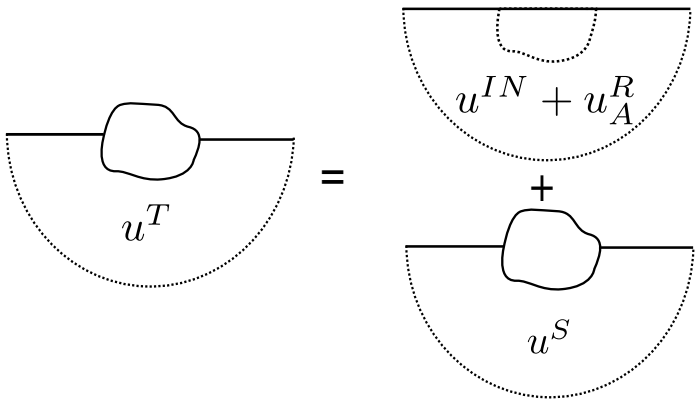

Figure 3.2. Classical partition of the total solution into free field plus scattered motions.

$$u^T = u^{IN} + u^R_P + u^D \equiv u^0_P + u^D \tag{3.2}$$

In analogy with the free-field motion u^0_A defined in Eq (3.1), we refer to the superposition $u^{IN} + u^R_P \equiv u^0_P$ as the physical incoming field.

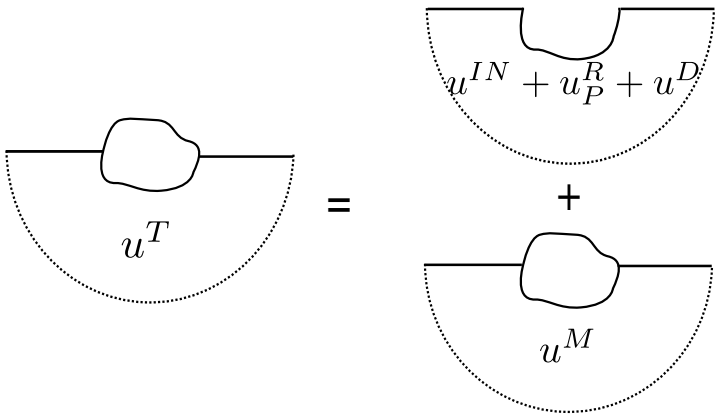

Figure 3.3. Partition of the solution into incident, physically reflected and diffracted fields.

If we now add the scatterer domain V_1 to the exterior half-space domain with free surface $S_F \cup S$, it will introduce an additional field u^M so the total final solution can be written like;

$$u^T = u^{IN} + u^R_P + u^D + u^M \equiv u^0_P + u^D + u^M \tag{3.3}$$

In contrast to Eq (3.1), the superposition in Eq (3.3) is physical, as it naturally separates the geometric contribution –represented by the term $u^R_P + u^D$– from that associated to the additional scattered motions u^M.

Assuming now that the total field u^T has been obtained (for instance, by a numerical method), a comparison between Eq (3.1) and Eq (3.3) yields the scattered displacements

$$u^M = u^T - u_P^0 - u^D. \tag{3.4}$$

If there is no scatterer (e.g., no impedance contrast), then $u^M = 0$ and there are only geometric modifications captured by the diffraction term u^D as;

$$u^D = u^T - u_P^0. \tag{3.5}$$

Notice that the general solution expressed by Eq (3.3) captures the unmodified half-space solution in which case we have that $u^M = u_A^0 - u_P^0 - u^D$ which results after writing

$$u^T = u_P^0 + u^D + u^M \equiv u_A^0. \tag{3.6}$$

In order to obtain the diffraction term as indicated by (3.5), the problem is first solved numerically while the term u_P^0 is obtained by geometrical means as described in Fig. 3.4 for a semi-circular shape. The reflection process is described after defining the radii of the circle R, the horizontal variable x, the dimensionless horizontal variable $\alpha = x/R$ ($\alpha \in [-1, 1]$) and the radial vector, which is expressed as $\mathbf{r} = (\alpha, \sqrt{1-\alpha^2})$.

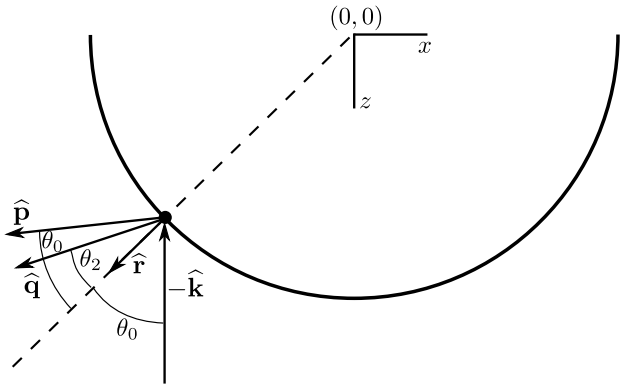

Figure 3.4. Geometrical theory solution for the semicircular canyon.

It follows that the angle θ between the vertical and the radial vector, for each point over the semicircle, reads

$$\theta = \operatorname{acos}\left(\sqrt{1 - \left(\frac{x}{R}\right)^2}\right) \quad .$$

The reflected rays giving the field term u_P^R are expressed in the general case as

$$\widehat{\mathbf{p}} = (2\alpha\sqrt{1-\alpha^2}, 1-2\alpha^2) \ ,$$
$$\widehat{\mathbf{q}} = (\text{sign}(\alpha)\sqrt{1-\cos^2(\theta_0+\theta_2)}, |\cos(\theta_0+\theta_2)|) \ ,$$

where

$$\theta_2 = \theta_{SV} = \text{acos}\left[\frac{\sin\theta}{v_r}\right],$$

for a P wave incidence, and

$$\theta_2 = \theta_P = \text{acos}\left[v_r \sin\theta\right],$$

for an SV wave incident and with $v_r = \alpha/\beta$ being the ratio between the primary and secondary waves speeds.

3.1.2 Scattering of P and SV waves by a semicircular and a rectangular canyon

In order to study the connection between the diffracted field and the topographic effect, we selected two simple problems. The first case corresponds to the semi-circular cylindrical canyon previously studied by Wong (1982) and Kawase (1988). That problem has two singular sources of diffraction located at the top rims of the canyon. As a second study case, we selected a canyon with a rectangular cross-section and four concentrated sources of diffraction located over the top and bottoms surfaces. In the case of oblique incidence both problems will also exhibit diffraction in the corresponding shadow zones.

The canyons are geometrically defined by their depth $H = 1.0Km$, width $B = 2.0Km$ (for the rectangular case) and radius $a = 1.0Km$ (for the semi-circular case). Note that in the rectangular canyon $a = B/2$. The half-space is mechanically described by a mass density $\rho = 1000Kg/m^3$, a velocity of shear wave propagation $\beta = 1.0Km/s$ and a Poisson's ratio $\nu = 1/3$. We performed two different sets of analysis regarding the frequency content of the incident waves. In a first analysis, we obtained the response of the canyons using a a Ricker pulse of central frequency $f_c = 1.0Hz$, maximum frequency $f_{max} = 4.0Hz$ and a time duration $T_{max} = 8.0s$. For this case we obtained the geometrical solution over the canyon surface, so we were able to compute also the diffracted field along this surface. In a second set of analysed cases we use a Ricker pulse of central frequency $f_c = 4.0Hz$, maximum frequency $f_{max} = 16.0Hz$. The purpose of this analysis was to obtained a time domain response of higher resolution so we were able to identify the different phases appearing in the computational domain. In both cases we considered incidence angles (defined with respect to the vertical) corresponding to $\theta = [0^0, 30^0]$. The analysis was conducted in the frequency domain with a frequency step of $\Delta f = f_{max}/32$ and $\Delta f = f_{max}/256$ in each

set of analysis. The model responses were studied for a normalized frequency $\eta = \omega a/\pi\beta$. The amplitude of the frequency domain transfer function associated to the diffracted field, was obtained from Eq.(3.5), after computing the total field u^T numerically, while the physically-based incoming field U_P^0, was obtained analytically.

Figure 3.5 displays the results corresponding to the case of an SV wave, incident at $\theta = 0^0$ and $\theta = 30^0$ over the rectangular canyon (columns 1 and 2) and semi-circular canyon (columns 3 and 4). Rows 1 to 3 correspond to the vertical displacements, while rows 4 trough 6 show the horizontal components. We show in each case, the spatial distribution of the transfer function at the normalized frequency $\eta = 1.0$ associated to the diffracted field, total field and the related synthetic seismograms along these same surfaces (rows 3 and 6). For the rectangular canyon the range of $x \in [-1.0, 1.0]$ corresponds to the bottom of the canyon, while $x >\| 1 \|$ corresponds to the canyon walls.

For the rectangular shape under vertical incidence, the diffraction effect is revealed by the large amplification near the rims of the canyon, where the amplitude of the transfer function corresponding to the vertical displacement component at $\eta = 1.0$ reaches a value close to 3.0. In this case, as the main incident front encounters the bottom corners of the canyon, these geometric singularities become sources of diffracted waves. From analytical solutions of the diffraction of a P wave by a slit (Achenbach, 1973), we know that such a singularity, generates head waves and P and SV diffracted waves. These last two exhibiting cylindrical fronts. In the current problem all these fronts propagate vertically over the canyon walls and horizontally over the bottom surface.

To reinforce the analysis we also show in Fig.3.6 snapshots of the propagation patterns at four different time instants. At $t = t_1$, the incident SV wave has already been diffracted by the corner singularities at the bottom of the canyon, producing cylindrical diffracted P and SV waves. Over the horizontal bottom surface, the leading diffracted P wave travels in phase with a head wave (required to match the traction free boundary condition). The diffracted SV wave follows along the same bottom surface and both (the P and the SV component) are tied by the head wave extending from the surface to the inside of the computational domain. Similarly, over the vertical walls and propagating upwards, one encounters the incident grazing SV wave, the cylindrical diffracted SV wave, the cylindrical diffracted P wave and a joining head wave. It is interesting to observe how the diffracted SV wave travelling alone over the bottom surface is enough to match the traction free boundary condition, while it is coupled to the incident front over the vertical wall.

The incident and diffracted cylindrical waves, generated after the first interaction with the bottom singularities, will also experience further diffraction as they encounter the opposite corners of the canyon. To clarify this aspect of the response, one could use Huygen's principle ideas to think of the bottom corners like sources of diffracted cylindrical and head waves. If we refer to this diffracted field as the primary diffraction, then it is clear that the primary diffracted field will experience further diffraction as it encounters the opposite corners located over the horizontal and vertical surfaces. This field should, by obvious reasons be termed the second order diffraction effect.

Eventually, the process of activation of Huygen's sources of diffracted waves continues indefinitely forcing energy to become trapped along the canyon surface in the form of higher order diffraction. This effect is observed in the synthetic seismograms and also from the snapshot at $t = t_2$, as the increase in duration of the signals over the bottom surface. The larger amplification at the canyon rims observed in the frequency domain resposne (see Fig. 3.5) is now evident since at these locations the incident, reflected and primary diffraction fields will converge.

An additional point of interest regarding the diffraction field, is observed in the response inside the computational domain in the snapshots at $t = t_3$ and $t = t_4$. In the first case, the cylindrical SV diffracted wave, propagates in phase with the first reflected field. It is observed how these two waves deplete each other as they move away from the canyon. In the second case, the diffracted field generated by the top corners, propagates together with the reflected wave, in such a way that it restores the front in the far field and as it moves away from the canyon. From these two opposite cases it is clear how the diffracted part of the response, has the ability to complete or deplete the field as required.

In the cases of incidence at 30^0 (columns 2 and 4 in Fig. 3.5), the propagation pattern is complicated since the incoming field is composed of 3 sets of rays leading to the activation of multiple diffraction sources. The first diffractor is activated when the incident SV wave, meets the corner singularity in the illuminated zone as depicted in the first snapshot from Fig.3.6. Once again the cylindrical diffracted P and SV waves are clearly identified. This primary diffraction must deplete, in the far field, the reflection of the P wave in the left-most canyon vertical wall. Similarly, in the snapshot at $t = t_2$ the main incident SV wave and its associated diffracted field, experiences second order diffraction by the right bottom corner, while the reflected P wave is undergoing its first order diffraction. In this case the cylindrical P and SV diffracted waves propagating over the horizontal surface, will diffract once again by the right bottom corner. In the snapshot at $t = t_3$, the diffraction of the main incident wave is already filling up the shadow zone and experiencing third order diffraction by the canyon top singularity. At that instant the reflected P wave is experiencing second order diffraction. Finally at $t = t_4$, the multiple diffracted waves are starting to complete the fronts of the free field, both in the shadow and illuminated zones.

A similar behaviour is observed in the case of the semi-circular canyon under a vertically incident field. For this problem the time domain response is depicted in the snapshots in Fig. 3.7. In the frame at $t = t_1$ the incident field has just been reflected in the form of SV and P waves. Along the canyon surface these three waves travel in phase, until they experience the first diffraction event as shown at $t = t_2$ where now the field is composed of the incoming wave plus the diffracted P, SV and head waves. At $t = t_3$ the diffracted field is approaching the edges where it will undergo second order diffraction. In that frame and at $t = t_4$ the reflected SV front is already being restored.

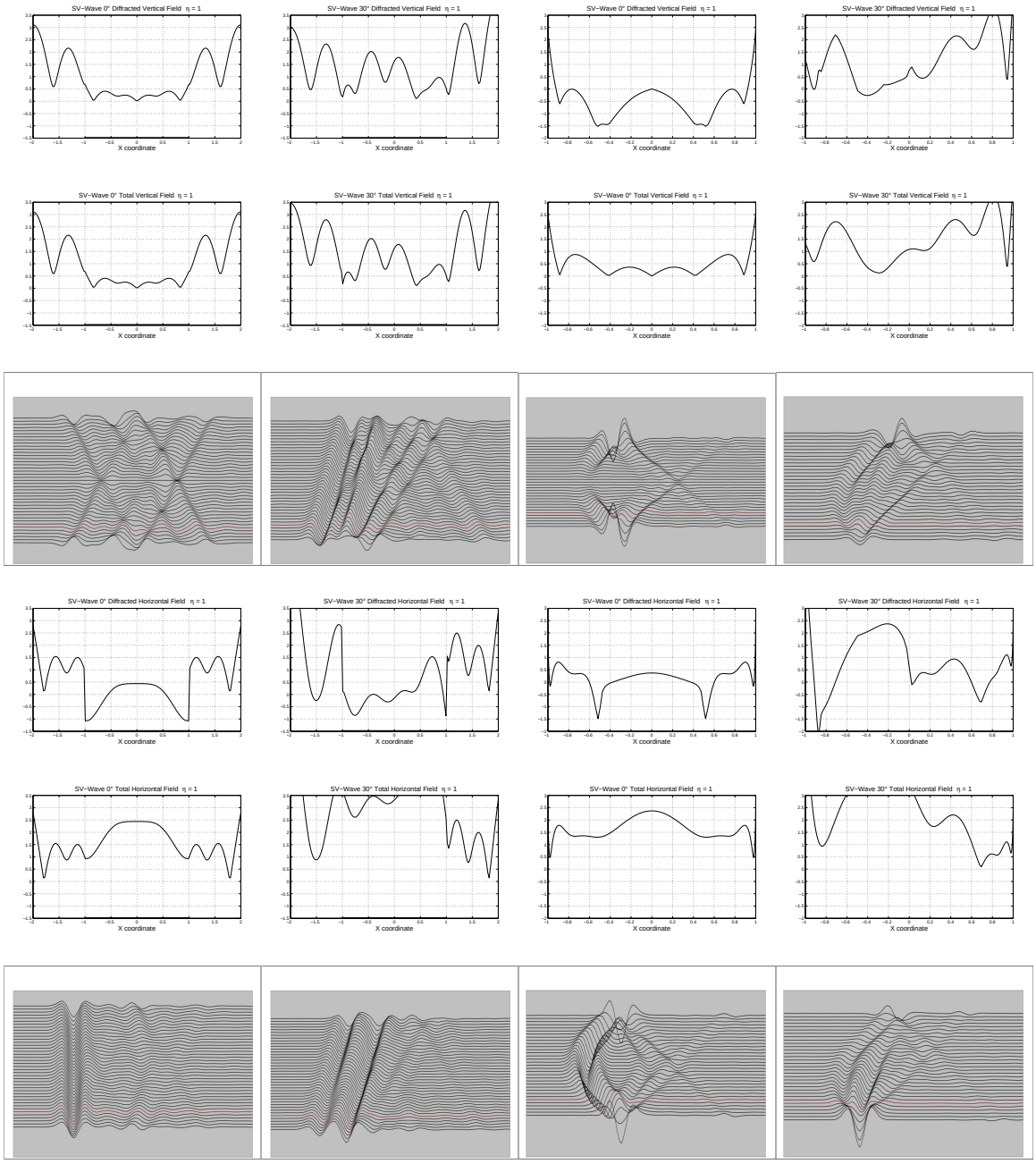

Figure 3.5. Response of the rectangular and semi-circular canyons to SV waves incident at $\theta = 0^0$ and $\theta = 30^0$. The results shown in rows 1 and 2 correspond to the spatial distribution over the free surface of the frequency domain transfer function at the characteristic frequency $f_c = 1.0Hz$ associated with the diffracted (row 1) and total (row 2) vertical displacement component. The results in row 3 are the synthetic seismograms over the canyon surface in each case. The first two columns correspond to the rectangular canyon and columns 3 and 4 to the circular canyon.

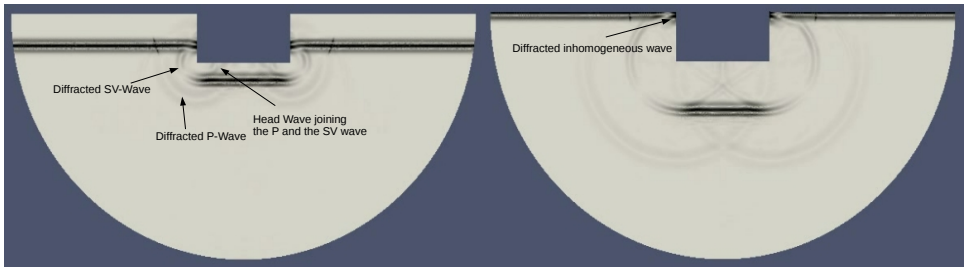

(a) $t = t_1$ **(b)** $t = t_2$

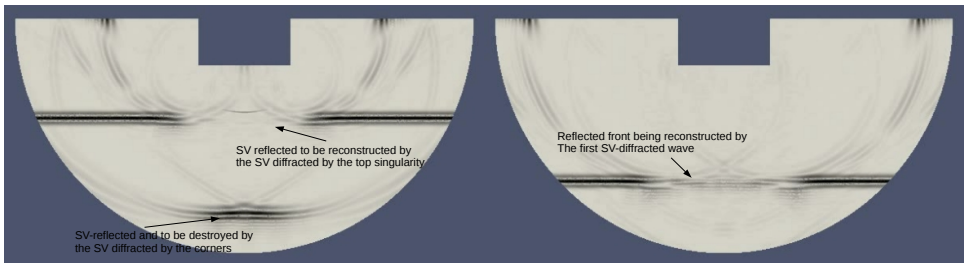

(c) $t = t_3$ **(d)** $t = t_4$

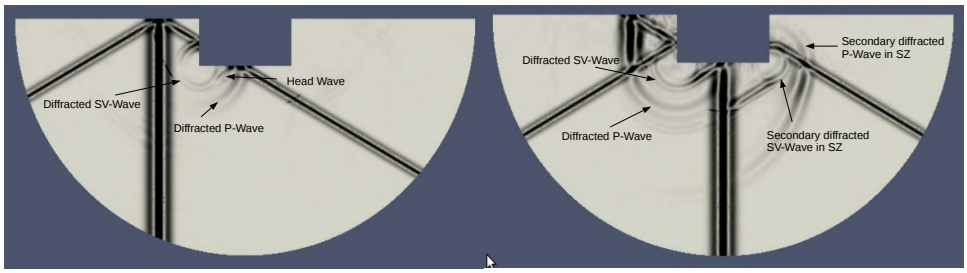

(e) $t = t_1$ **(f)** $t = t_2$

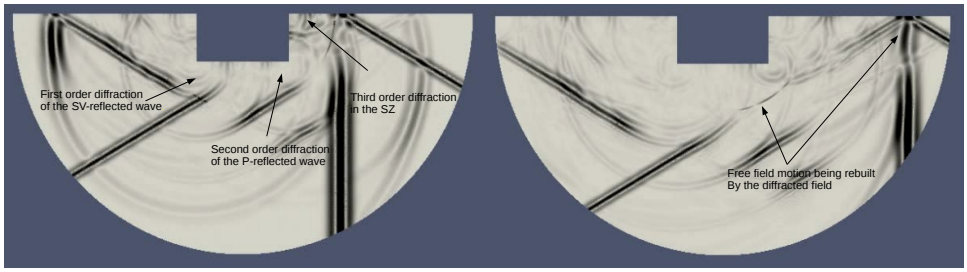

(g) $t = t_3$ **(h)** $t = t_4$

Figure 3.6. Response of the rectangular canyon to a vertically and a 30^0 incident SV wave. The snapshots correspond to full particle motions. The full videos are available at `http://www.youtube.com/watch?v=gen5mNxJPiw` and `http://www.youtube.com/watch?v=NdijUjEWfAI&feature=youtu.be`

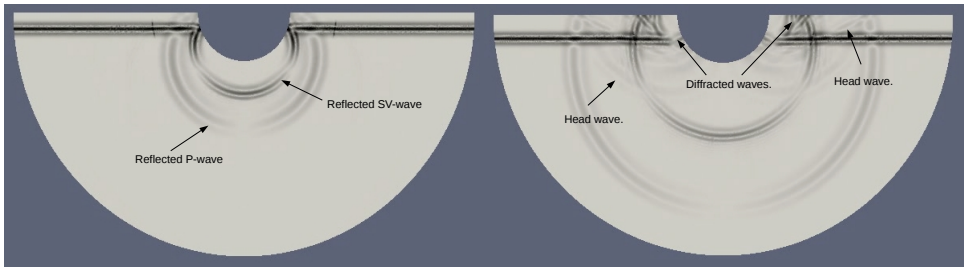

(a) $t = t_1$ **(b)** $t = t_2$

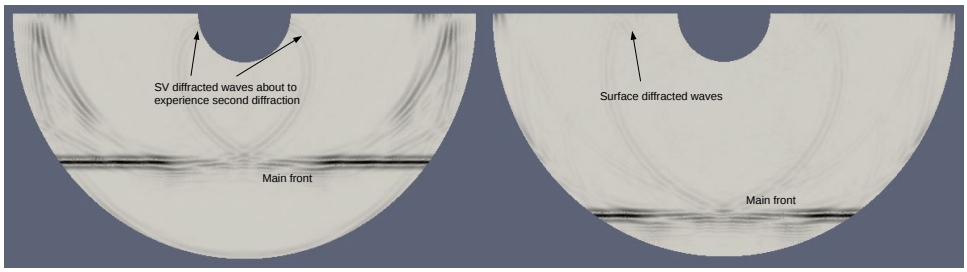

(c) $t = t_3$ **(d)** $t = t_4$

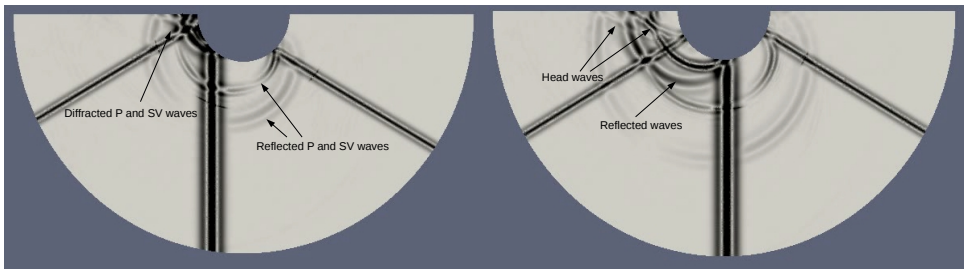

(e) $t = t_1$ **(f)** $t = t_2$

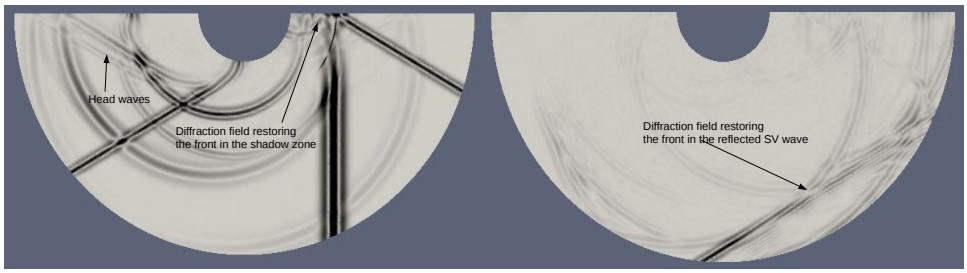

(g) $t = t_3$ **(h)** $t = t_4$

Figure 3.7. Response of the semi-circular canyon to a vertically and a 30^0 incident SV wave. The snapshots correspond to full particle motions. The full videos are available at `http://www.youtube.com/watch?v=tlCKdgmioGY&feature=youtu.be` and `http://www.youtube.com/watch?v=qcq-WYMEvSY&feature=youtu.be`

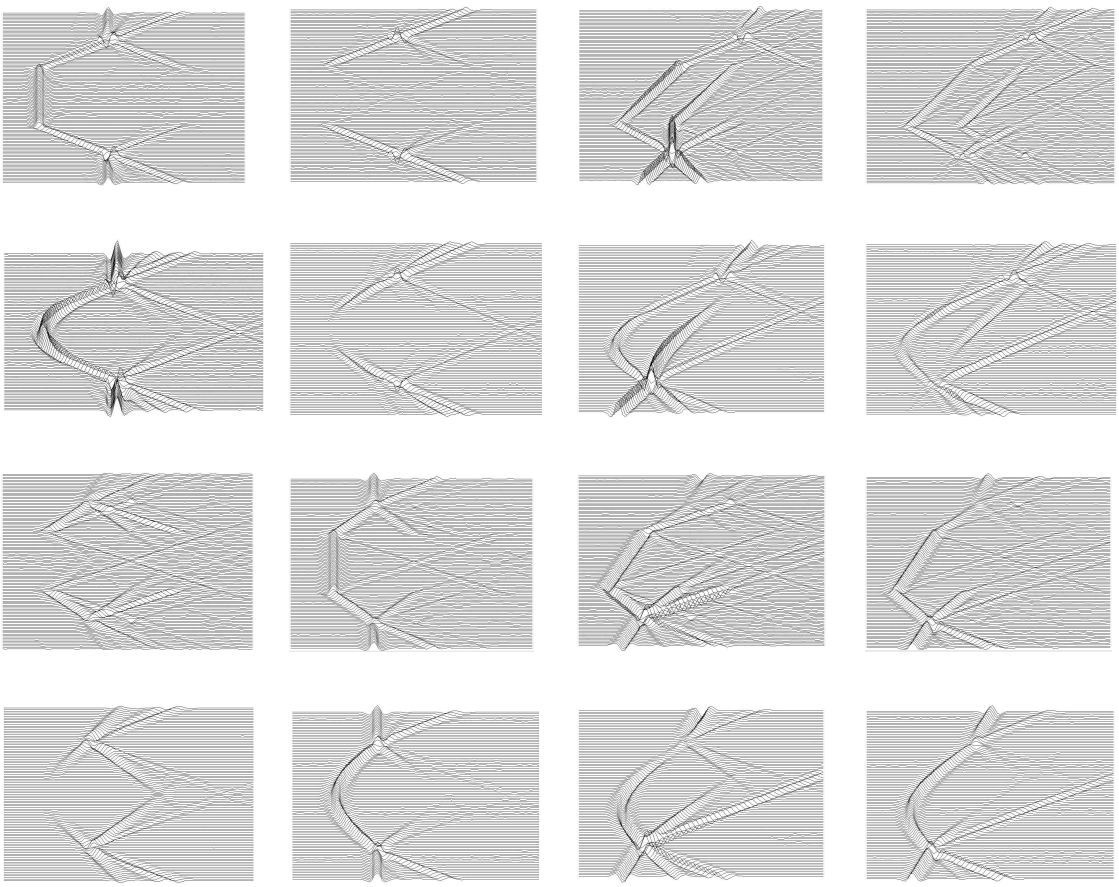

Figure 3.8. Synthetic seismograms for the semi-circular and rectangular canyon under incident SV and P waves. Row 1 correspond to the SV case in the rectangular canyon. Row 2 correspond to the SV case semi-circular canyon. Row 3 correspond to the P case in the rectangular canyon. Row 4 correspond to the P case in the semi-circular canyon. Columns 1 and 2 depict the horizontal and vertical field for 0.0^0 incidence while columns 3 and 4 depict the horizontal and vertical fields for 30.0^0 incidence.

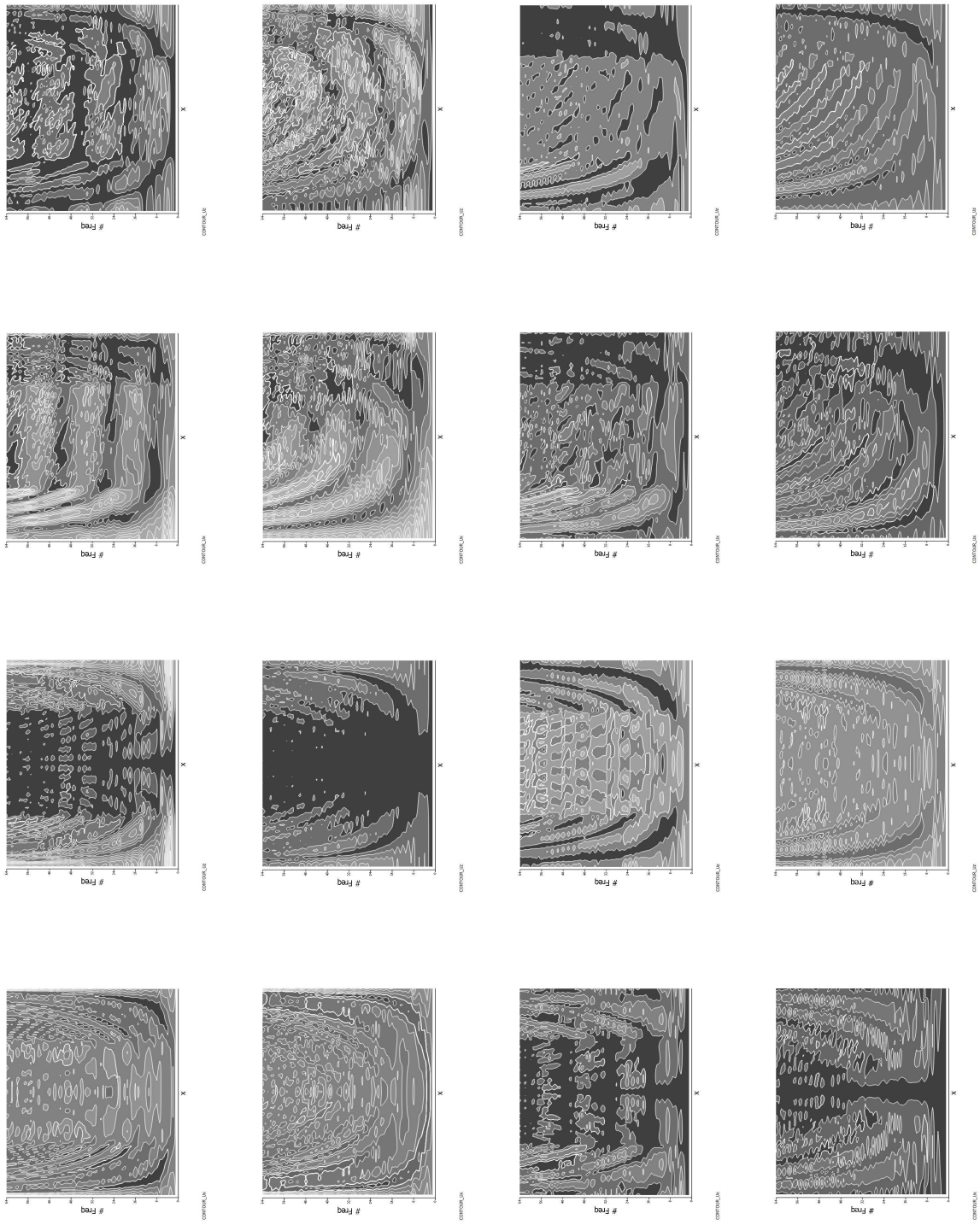

Figure 3.9. Transfer functions for the semi-circular and rectangular canyon under incident SV and P waves. Row 1 correspond to the SV case in the rectangular canyon. Row 2 correspond to the SV case semi-circular canyon. Row 3 correspond to the P case in the rectangular canyon. Row 4 correspond to the P case in the semi-circular canyon. Columns 1 and 2 depict the horizontal and vertical field for 0.0^0 incidence while columns 3 and 4 depict the horizontal and vertical fields for 30.0^0 incidence.

3.2 The modified domain reduction method: Application to topographic effects

3.2.1 The domain reduction method

The procedure used previously to determine the diffracted part of the motion u^D corresponds to a particularization of the two-step algorithm proposed by Bielak et al. (2003), in the so-called domain reduction method (DRM). That approach was originally formulated as a means to effectively translate the excitation due to a seismic source existing in the far field of a large computational domain, to the vicinity of a localized region. In our current implementation, the DRM technique was used to progressively construct the solution to a complex problem by adding domain parts and its related fields. In our particular case, we expressed the total solution u^T to a scatterer problem after using the superposition given by Eq (3.3) which is repeated here for completeness in Eq (3.7);

$$u^T = u^{IN} + u^R_P + u^D + u^M \equiv u^0_P + u^D + u^M. \tag{3.7}$$

In this section we use the DRM technique as analysis tool to address the problem of site effects where we use the superposition process stated in Eq (3.7) to separate the regional effects from the truly local effect. In particular, the question we try to answer is the following: If we want to capture the local effects at a site, say where a building is to be designed then Â¿ what is the proper extension of the computational domain that must be considered in order to make a realistic prediction of those effects? To clarify our idea further, consider the schematic representation of Figure 3.10. Suppose that in that representation the problem consists in determining the site effects at a micro-zone of a sedimentary valley, that at the same time is supported by a half-space representing the bedrock.

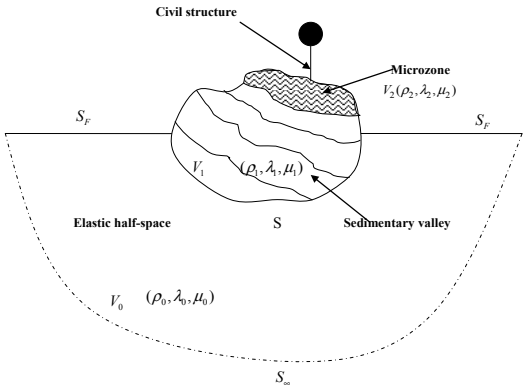

Figure 3.10. Full domain considering a structure and a micro-zone.

In our proposed approach we perform a first analysis step, where we solve the scatterer problem for a reduced version of the model shown in Figure 3.11, including the half-space and sedimentary valley, but with the micro-zone and structure being removed. We denote the results from that analysis like u_R^0. This term will be referred to like the regional effect.

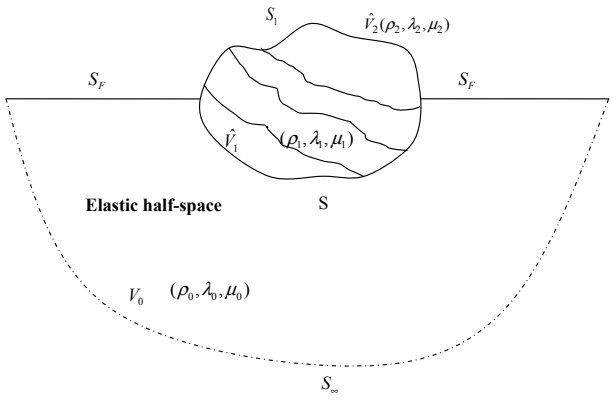

Figure 3.11. Reduced domain with the micro-zone and structure being removed.

In a second analysis step, we take the results corresponding to u_R^0, which have been previously stored in the vicinity of the micro-zone, and use them as an effective seismic excitation to study the local response at the site as depicted in Figure 3.12

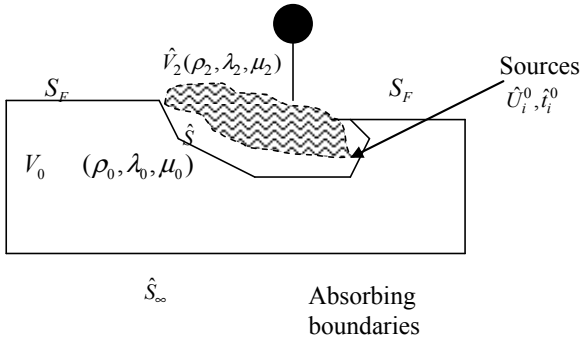

Figure 3.12. Final domain for the micro-zone excited with the response from the reduced domain.

The two step algorithm can be written like;

$$u^T = u_0^R + u_{MZ} \tag{3.8}$$

where u_{MZ} corresponds to the response in the microzone.

3.2.2 Application to topographic effects.

In this section the modified domain reduction method is applied in the analysis of the simplified topography depicted in Figure 3.13. It is composed of a large canyon, resembling a typical cross section of the Aburra sedimentary basin, and a localized softer soil deposit with circular shape, representing a typical microzone. The canyon is $10.0Km$ wide $\times$ $1.0Km$ deep in its central point. The bedrock material has a mass density $\rho = 1.0Kg/m^3$, a shear wave propagation velocity $\beta = 1.0Km/s$ and a Poisson's ratio $\nu = 1/3$. The localized soil deposit, on the other hand, is $600m$ wide $\times$ $100m$ deep in its central point, while it has a mass density $\rho = 1.0Kg/m^3$, a shear wave propagation velocity $\beta = 0.5Km/s$ and a Poisson's ratio $\nu = 1/3$. The purpose of the analysis is to identify the incidence of the regional effect in the localized response of the micro-zone and to answer the question of whether or not that regional effect can be determined for a given region. For that purpose we conduct three different analysis as explained next.

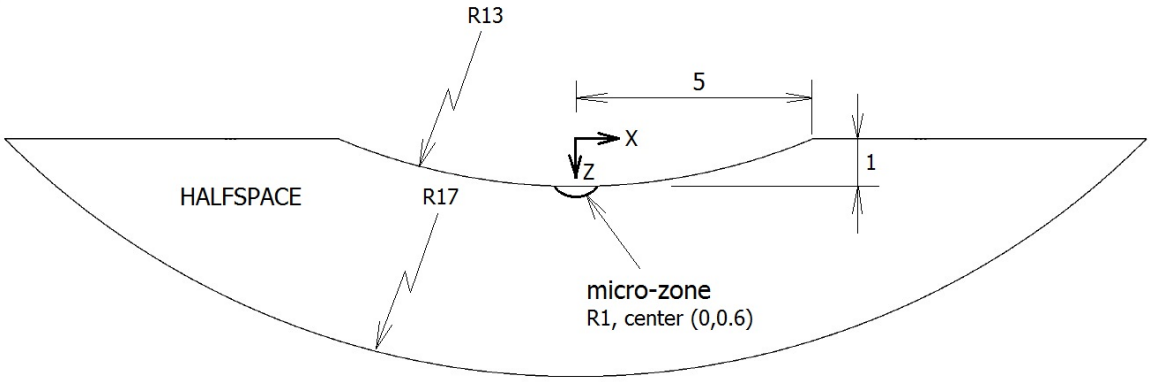

Figure 3.13. Simplified model equivalent to the Aburrá valley with a localized soil deposit.

In a first step the full model is submitted to a vertically incident SV wave. This solution is regarded as the exact referent solution. In an intermediate step, we solve the canyon for the same vertically incident SV wave, but with the localized micro-zone being removed. The field resulting from this analysis is stored as a database of effective excitations at a set of points where micro-zones are expected to be located. We refer to this intermediate solution as the regional solution. Figure 3.14 shows a set of points near a micro-zone where the regional solution is to be stored.

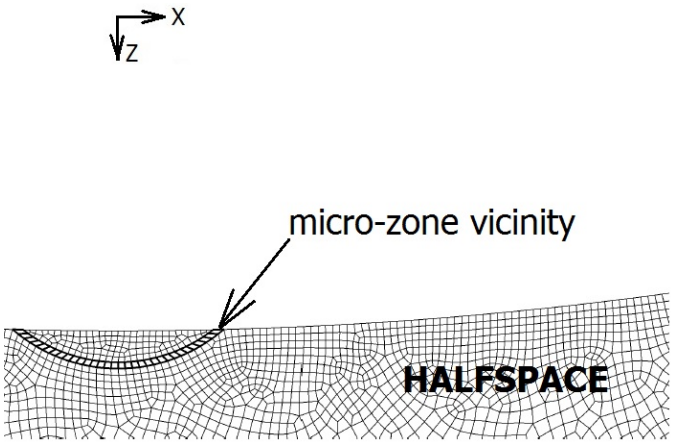

Figure 3.14. Set of points near a microzone where the regional solution is stored.

In a second analysis step, referred herein as the local or reduced domain (DRM) model, the micro-zone is assumed to be located over a homogeneous half-space, without regional topography, see Figure 3.15. The local model is then solved with the field obtained from the regional model as excitation.

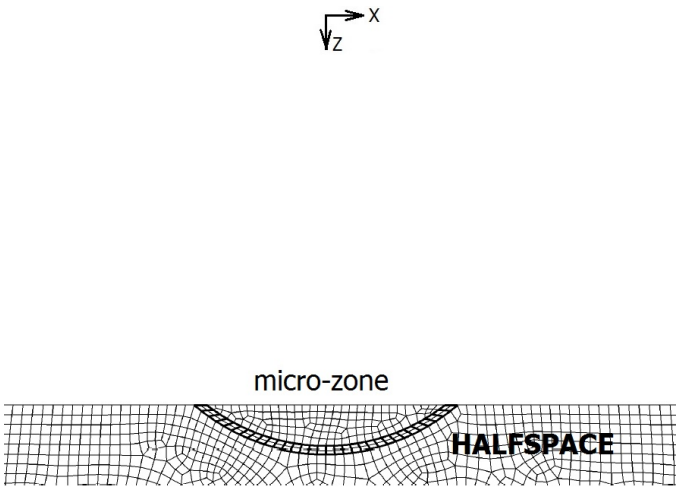

Figure 3.15. Local model of the microzone.

The third and final analysis step, is intended to represent what is known to be a common practice by engineers at a consulting office and where the microzone is described as a stack of layers of different heights and material properties, assumed of infinite lateral extension and supported by a rigid bedrock. The simplified model is then subjected to accelerations at the base in order to determine the surface response. Here, instead of following the engineer's one-dimensional approach, we consider the local model (see Figure 3.15) and determine its response to a vertically incident SV wave. This third analysis is termed here the classical analysis.

All the analysis were conducted for a Ricker pulse of central frequency $f_c = 2.0Hz$, maximum frequency $f_{max} = 8.0Hz$, extent of the time window $T_{max} = 16.0s$ and a frequency increment corresponding to $\Delta f = f_{max}/128$. In terms of the non-dimensional frequency defined like $\eta = 2 \times a/\lambda$ these values correspond to $\eta_c = 2.4$ and $\eta_{max} = 9.6$. In order to determine the incidence of the regional effect at the localized microzone, we compare in Figure 3.16 the spatial distribution of the transfer function for the horizontal and vertical component of the system at $\eta = [1.2, 1.92, 3.125]$. From the results in the frequency domain, it is apparent that at least for the central location of the micro-zone the regional effect is minimum, and the response at the central point is mainly controlled by the mechanical effect. This may be explained by the symmetry of the canyon and the fact that at the midpoint there is destructive interference of the diffracted motions.

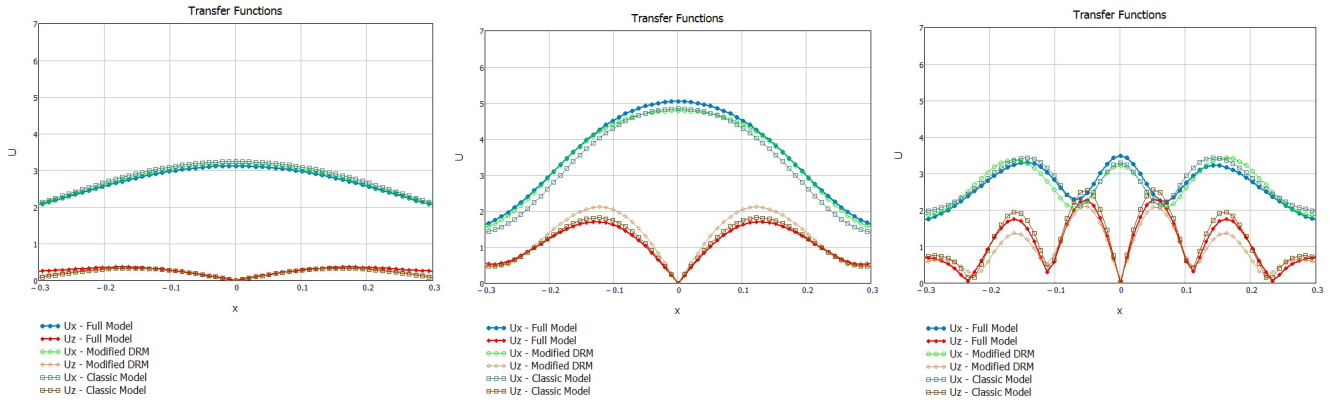

(a) $\eta = 1.20$ **(b)** $\eta = 1.92$ **(c)** $\eta = 3.12$

Figure 3.16. Spatial distribution of the frequency domain transfer functions for the horizontal and vertical component of the response at three different values of the non-dimensionless frequency η for receivers located over the microzone surface.

In Figure 3.17 we also compare the Fourier spectral amplitude for the horizontal displacement component at the midpoint. Once again, there is no difference between the results from the three models providing additional evidence to the results obtained with the spatial transfer functions.

As a final verification Figure 3.18 compares the synthetic seismograms from the three analysis. It is observed that the classical (or engineer model) underpredicts the displacement amplitude and modifies the frequency content during the intense phase of the seismogram. From a physical point of view, in the full model, which is representative of the realistic scenario, there are infinite diffracted waves trapped between the rims of the canyon. These waves are neglected in the classical model, however from the excellent agreement observed between the full and reduced model it is evident that this diffraction effect is effectively carried by the excitation obtained with the regional model.

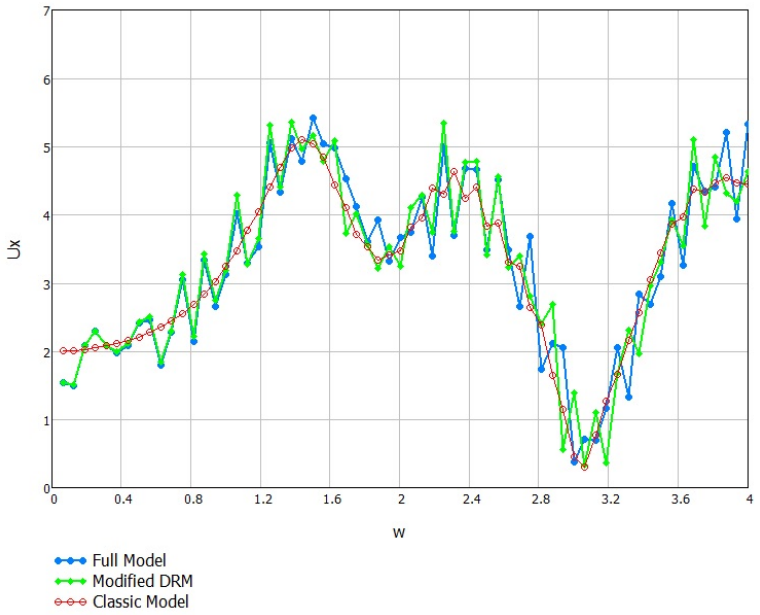

Figure 3.17. Fourier spectral amplitude at the central point of the microzone obtained with the complete model, DRM-model and classical model.

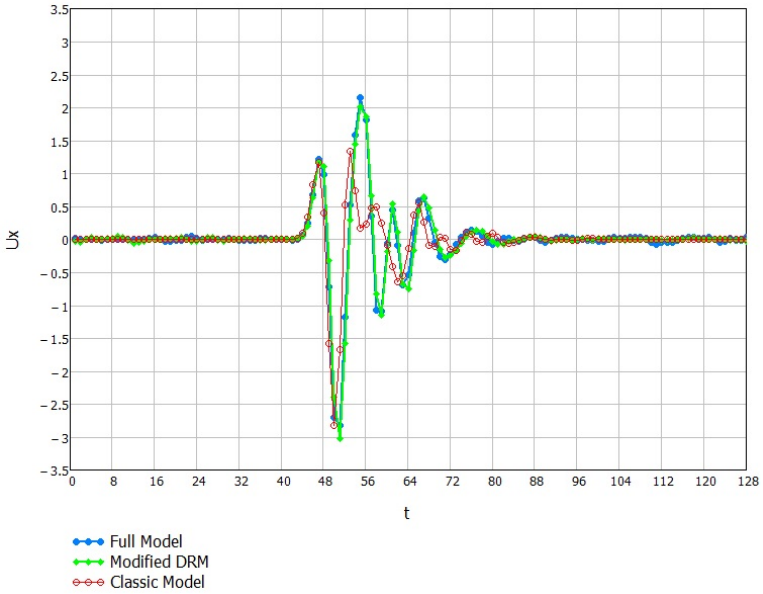

Figure 3.18. Synthetic seismograms at the central point of the microzone obtained with the complete model, DRM-model and classical model.

In order to consider a possible worse case scenario to objectively asses the potential benefits of the DRM method as analysis tool to study site effects a second analysis was performed. In

particular, a second microzone was considered, but now located near one of the diffraction sources of the canyon. The complete model is described in Figure 3.19. For this analysis the classical (or engineer) model of the microzone since the engineer always sees the soil deposit as resting on a half-space with flat surfaces and with vertically incident waves.

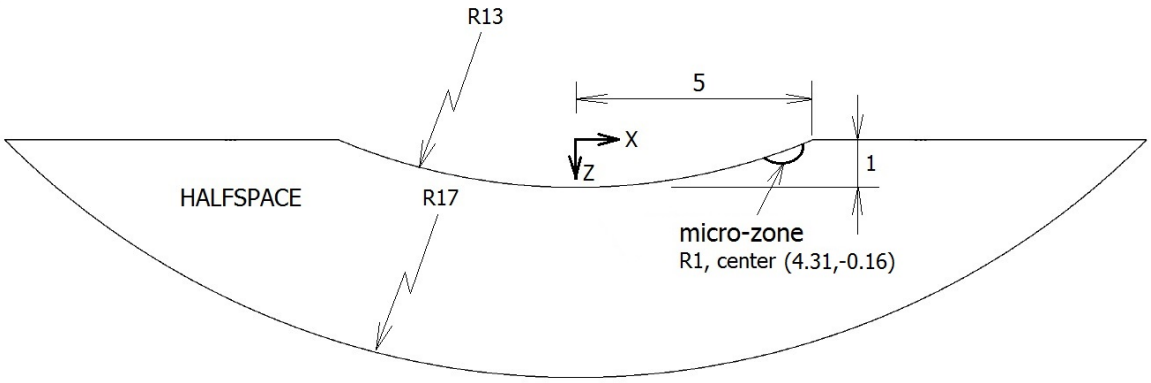

Figure 3.19. Simplified model equivalent to the Aburrá valley with a localized soil deposit.

The same set of results obtained in the first model is also presented. Figure 3.20 depicts the spatially distributed transfer functions, Figure 3.21 the Fourier spectral amplitude and Figure 3.22 the synthetic seismograms from the three considered methods. The agreement between the results from the full model and the reduced domain method is almost exact, while the results from the classical model exhibit significant differences. The classical model captures only the natural frequency of the microzone, which is in part dominated by the mechanical effect. The classical model however underpredicts the amplitude associated to the natural mode. From the analysis conducted in section 4.1 it is known that near the edges of the canyon large amplifications due to the diffraction effect should be generated. This diffraction effect, which is effectively being captured by the regional model, and subsequently applied to the reduced model seems to be the most relevant aspect of the excitation and the mechanical effect appears to play a minor role in the local response. In a more detailed study a separation of the geometric effects contained in the regional model and the mechanical effects, contained in the micro-zone, should be conducted. That study should provide correction factors to be applied to the standard one-dimensional models to account for the geometric effect.

The excellent agreement between the full and reduced domain results, suggest that the DRM technique should be explored in more detail as a potential tool to study the problem of site effects. In particular this method seems promising to be used, not only in the study of the physical problem, but also as a tool to extract useful results from large scale simulations. This idea will be further explored in the near future inside the Mecanica Aplicada Lab at Universidad EAFIT.

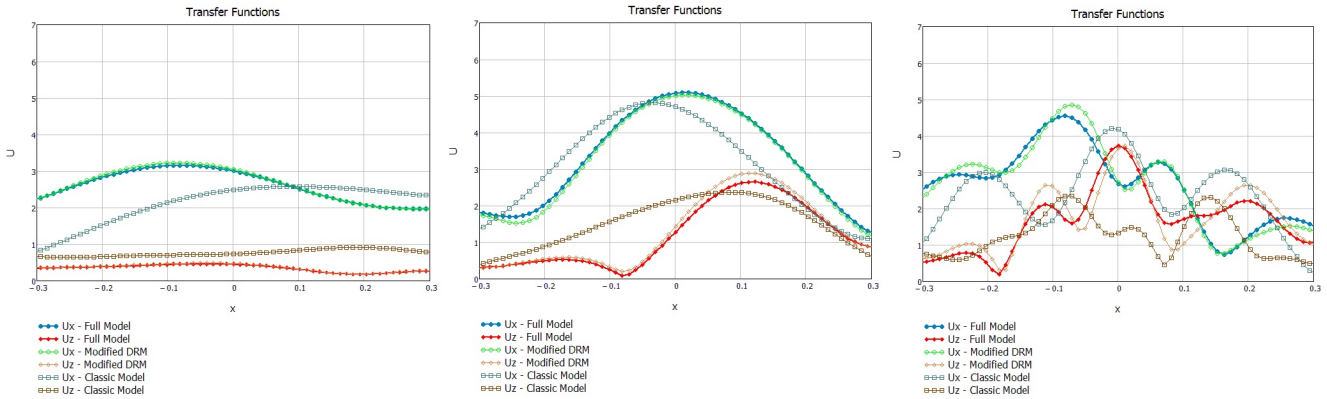

(a) $\eta = 1.20$ **(b)** $\eta = 1.92$ **(c)** $\eta = 3.12$

Figure 3.20. Spatial distribution of the frequency domain transfer functions for the horizontal and vertical component of the response at three different values of the non-dimensionless frequency η for receivers located over the inclined microzone surface.

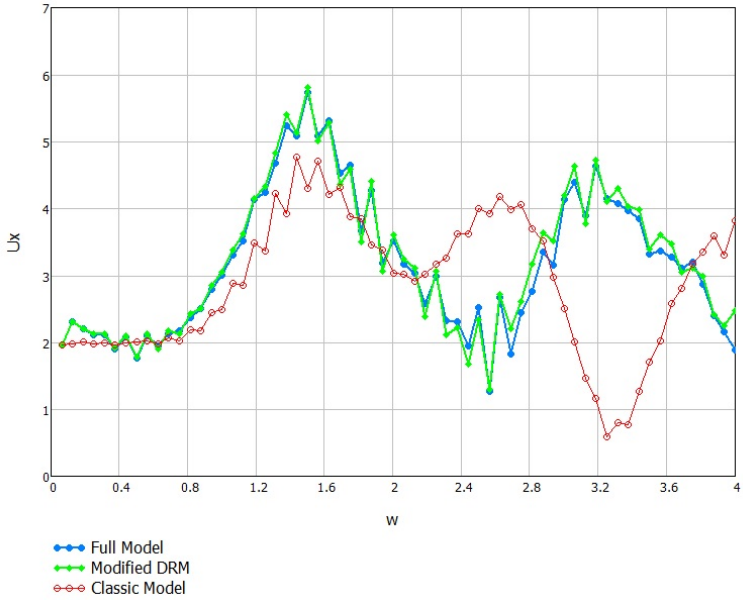

Figure 3.21. Fourier spectral amplitude at the central point of the microzone obtained with the complete model, DRM-model and classical model for the second microzone.

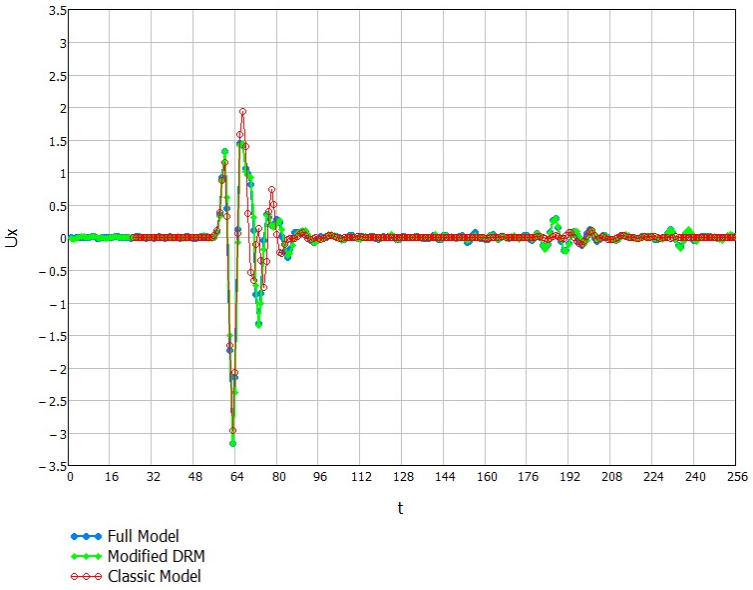

Figure 3.22. Synthetic seismograms at the central point of the microzone obtained with the complete model, DRM-model and classical model for the second microzone.

Chapter 4

Scattering in a Micropolar Solid

Introduction

At high frequencies, materials with micro-structure exhibit dispersive behaviour and the velocity of wave propagation becomes frequency dependent. As a result, a travelling pulse becomes distorted as it propagates. This may be interpreted as a micro-scattering effect, triggered when the wavelengths of the incident field and the characteristic dimensions of the micro-structural features, become of comparable size. The study of dispersive media is of interest in different applications like, damage detection, non-destructive testing, rotational seismology, geotechnical engineering, etc. This behaviour can be captured in numerical simulations through two different approaches. First, explicitly including the micro-structural details in the computational solution of a classical continuum model and second, using a non-classical continuum model.

Although the original idea of considering the micro-structure with enriched media was due to Voigt (1910), the most prominent contribution to the field was due to Cosserat & Cosserat (1909) who proposed the addition of rotational interactions between the material points in the continuum manifold. Models inspired on the Cosserat's idea flourished during the 1950's and 1960's (Truesdell & Toupin (1960), Toupin (1962), Mindlin & Tiersten (1963), Koiter (1964), Mindlin (1964), Mindlin (1965), Aero & Kuvshinskii (1961), Mindlin & Eshel (1965), Eringen (1966)) with special interest given to the description of observations of wave dispersion relations at long wave lengths in the theory of crystal lattices and in neutron scattering experiments made by Brockhouse & Huang (1958) Brockhouse and Iyengar (1958) and Gazis and Wallis (1962) Gazis & Wallis (1962). At the same time, some experimental work was conducted by Lakes (1982) who performed torsional resonant experiments on wet compact human bones to determine Cosserat material parameters. He found length scales comparable in size to that of osteons.

Studies related to infinite and semi-infinite non-classical media, including the derivation of re-

flection/refraction coefficients, Green's functions for full-spaces and radiation boundary conditions, were performed by Parfitt & Eringen (1969), Airman (1972), Khan et al. (1971), Ignaczak (1972), Tomar & Cogna (1995) and Tomar et al. (36). Similarly, and after the recent development of seismic instruments capable of measuring rotations at a single point, interest was reborn in the study of wave propagation in non-classical media in what has been referred to as rotational seismology (Twiss et al. (1993);Takeo & Ito (1997), Takeo (1998a) and Takeo (1998b), Midya (2004), Kulesh et al. (2005), Teisseyre & Gorski (2009), Kulesh et al. (2006), Kulesh et al. (2005), Igel et al. (2007), Papargyri-Beskou et al. (2009), Gonella & Ruzzene (2007)).

In a non-classical model the material is still assumed to be homogeneous and the presence of the micro-structure is considered through additional degrees of freedom or higher order kinematic effects. In this chapter we use the micro-polar continuum model from Cosserat & Cosserat (1909) to consider dispersion. This frequency dependence of the propagation velocities requires the simulation of plane waves to proceed in the frequency domain. The dispersive properties in the Cosserat model are introduced through the addition of rotationally independent extra-degrees of freedom. This kinematic enrichment gives rise to an additional propagation mode in the form of micro-rotational waves, which become coupled to the (SV) shear waves. This dispersive property of the medium is shown in Fig. 4.1.

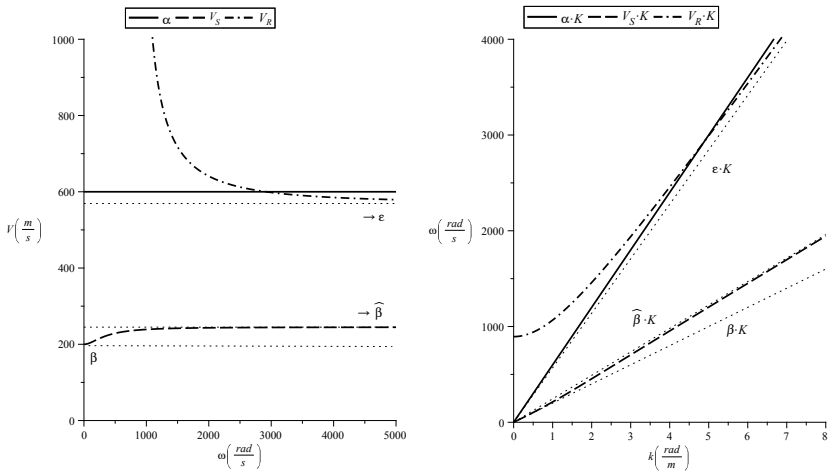

Figure 4.1. Dispersion for the micropolar waves.

As discussed above, in the case of dispersive media, the plane wave assumption requires the simulation to proceed in the frequency domain since each phase must be treated independently before synthesizing the response back to the time domain. In this chapter we first derive general finite element equilibrium equations for a micropolar model. By contrast with a classical model problem, where discrete equilibrium is stated in terms of nodal forces, in the case of a micropolar solid there are also nodal equilibrium relations in terms of nodal moments. The general formulation is then implemented into our user element subroutine to address the diffraction by a semi-circular canyon embedded in a micropolar half-space.

4.1 Non-classical Cosserat micropolar material

Consider a micro-polar elastic solid defined by Lame classical paramters λ and μ, by Cosserat paramters μ_c, γ and ξ and by mass and micro-inertia densities ρ and J respectively. For description of the micropolar model the reader is referred to Cowin (1970). In a micropolar solid in addition to the macro-rotations or asymmetric component of the displacement gradient tensor, there are also independent rotational degrees of freedom θ_i at each material point. As a result, the continuum model is now endowed with additional dynamic and kinematic modes, describing rotational interaction between the material points. The equilibrium equations for the 2D plane strain case are given in Eringen (1966), Kulesh (2006) and Cowin (1970) among others, and we just define the generalized stress and strain tensors to be used in the generalized finite element implementation described in the previous chapter. Denote the displacements and Cosserat micro-rotation vectors at a field point $\vec{x}$ and a the time instant t by $u_i(\vec{x},t)$ and $\theta_i(\vec{x},t)$ respectively and assume that $u_i(\mathbf{x},t) = u_i(\mathbf{x})e^{-i\omega t}$ and $\theta_i(\mathbf{x},t) = \theta_i(\mathbf{x})e^{-i\omega t}$.

The associated kinematic variables in a micropolar solid are given by ϵ_{ij}, γ_{ij}^A and κ_{ij}, corresponding to the classical infinitesimal strain tensor, the antisymmetric part of the relative deformation tensor (i.e., the difference between the displacement gradient and the micro-displacement gradient) and the curvature tensor. At the same time, the relevant stress variables are defined by τ_{ij} =classical symmetric Cauchy stress tensor, σ_{ij} =relative force stress tensor (with $\Sigma_{ij} = \tau_{ij} + \sigma_{ij}$ =total force per unit surface stress tensor), μ_{ij} =Cosserat couple stress tensor, $t_i = \Sigma_{ij}\hat{n}_j$ =force per unit surface tractions vector, $m_i = \mu_{ij}\hat{n}_j$ =couple per unit surface tractions vector, $\hat{n}_j$ =outward surface normal vector. The following principle of virtual work for a Cosserat solid, see Cowin (1970) can be derived;

$$\int_V \tau_{ij}\delta\epsilon_{ij}dV + \int_V \sigma_{ij}\delta\gamma_{ij}^A dV + \int_V \mu_{ij}\delta\kappa_{ij}dV - \int_S t_i\delta_i dS - \int_S m_i\delta\theta_i dS - \rho\omega^2\int_V u_i\delta u_i dV - J\omega^2\int_V \theta_i\delta\theta_i dV = 0. \tag{4.1}$$

The real part of the constitutive tensor relating stress quantities to strain quantities in the micro-polar solid is defined like;

$$\hat{M} = \begin{bmatrix} \lambda+2\mu & \lambda & \lambda & 0 & 0 & 0 & 0 \\ \lambda & \lambda+2\mu & \lambda & 0 & 0 & 0 & 0 \\ \lambda & \lambda & \lambda+2\mu & 0 & 0 & 0 & 0 \\ 0 & 0 & 0 & \mu+\mu_c & \mu-\mu_c & 0 & 0 \\ 0 & 0 & 0 & \mu-\mu_c & \mu+\mu_c & 0 & 0 \\ 0 & 0 & 0 & 0 & 0 & \gamma & 0 \\ 0 & 0 & 0 & 0 & 0 & 0 & \gamma \end{bmatrix} \tag{4.2}$$

4.2 Finite Element formulation

Define the displacement and micro-rotation interpolation functions like ${}_uN_i^k$ and ${}_\theta N_i^k$, where the superscript k makes reference to the contribution from the $k-th$ node of a given element. Using these functions we can write for the interpolated displacements and micro-rotations vectors at a given point inside the element the following relationships in terms of the k-th nodal variables u^k and θ^k;

$$u_i = {}_uN_i^k u^k, \quad \theta_i = {}_\theta N_i^k \theta^k \ . \tag{4.3}$$

It is convenient to express the micro-rotation vector θ_i in terms of its dual anti-symmetric rotation tensor θ_{ij} with the aid of the permutation tensor e_{ijk} as

$$\theta_{ij} = e_{qij}\ {}_\theta N_q^k \theta^k \equiv R_{ij}^k \theta^k \ .$$

Interpolation relationships for the derivatives of the primary fields u_i and θ_i follow

$$\begin{aligned} \epsilon_{ij} = B_{ij}^k u^k, \quad \omega_{ij} = \hat{W}_{ij}^k u^k, \\ \kappa_{ij} = M_{ij}^k \theta^k, \quad \gamma_{ij}^A = \hat{W}_{ij}^k u^k + R_{ij}^k \theta^k. \end{aligned} \tag{4.4}$$

where the tensor ω_{ij} denotes the anti-symmetric part of the displacement gradient. Substitution of (4.3) and (4.4) in (4.1) yields the PVW in terms of virtual nodal variables

$$\begin{aligned}\delta u^k \int_v B^k_{ij}\tau_{ij}dV + \delta u^k \int_V \hat{W}^k_{ij}\sigma_{ij}dV + \delta\theta^k \int_V R^k_{ij}\sigma_{ij}dV \\ +\delta\theta^k \int_V M^k_{ij}\mu_{ij}dV - \rho\omega^2\delta u^k \int_V {}_uN^k_i u_i dV - J\omega^2\delta\theta^k \int_V {}_\theta N^k_i\theta_i dV \\ -\delta u^k \int_S {}_uN^k_i t_i dS - \delta\theta^k \int_S {}_\theta N^k_i m_i dS = 0 \ .\end{aligned} \tag{4.5}$$

Using the arbitrary character of the virtual fundamental fields δu^k and $\delta\theta^k$ in (4.5), gives the following set of weak equilibrium equations in terms of nodal forces and nodal moments consistent with the stresses and couple stresses;

$$\begin{aligned}\hat{f}^k_\tau + \hat{f}^k_\sigma - \hat{f}^k_I - \hat{T}^k = 0 \\ \hat{m}^k_\sigma + \hat{m}^k_\mu - \hat{m}^k_I - \hat{q}^k = 0.\end{aligned} \tag{4.6}$$

Introducing the constitutive relationships

$$\begin{aligned}\Sigma_{ij} = C_{ijkl}\epsilon_{kl} + G_{ijkl}\gamma^A_{kl} \\ \mu_{ij} = D_{ijkl}\kappa_{kl}\end{aligned} \tag{4.7}$$

where C_{ijkl}, G_{ijkl} and D_{ijkl} are the micro-polar elasticity tensors, allow us to write the equilibrium statements (4.6) in matrix form as

$$\begin{bmatrix} K^{kp}_{uu} & K^{kp}_{u\theta} \\ K^{kp}_{\theta u} & K^{kp}_{\theta\theta} \end{bmatrix} \begin{Bmatrix} u^p \\ \theta^p \end{Bmatrix} - \omega^2 \begin{bmatrix} M^{kp}_{uu} & 0 \\ 0 & M^{kp}_{\theta\theta} \end{bmatrix} \begin{Bmatrix} u^p \\ \theta^p \end{Bmatrix} = \begin{Bmatrix} f_{ext} \\ q_{ext} \end{Bmatrix} \tag{4.8}$$

and where the following definitions apply:

$$K^{kp}_{uu} = \int_V B^k_{ij}C_{ijkl}B^p_{kl}dV + \int_V \hat{W}^k_{ij}G_{ijkl}\hat{W}^p_{kl}dV \equiv \int_V B^k_{ij}C_{ijkl}B^p_{kl}dV + \int_V \mu_c\hat{W}^k_{ij}\hat{W}^p_{ij}dV \ ,$$

which is symmetric.

$$K_{u\theta}^{kp} = \int_V \hat{W}_{ij}^k G_{ijkl} R_{kl}^p dV \equiv \int_V \mu_c \hat{W}_{ij}^k R_{kl}^p dV$$
$$K_{\theta u}^{kp} = \int_V R_{ij}^k G_{ijkl} \hat{W}_{kl}^p dV \equiv \int_V \mu_c R_{ij}^k \hat{W}_{kl}^p dV \ ,$$

with $K_{u\theta}^{kp} = \left(K_{\theta u}^{kp}\right)^T$.

$$K_{\theta\theta}^{kp} = \int_V R_{ij}^k G_{ijkl} R_{kl}^p dV + \int_V M_{ij}^k D_{ijkl} M_{kl}^p dV \equiv \int_V \mu_c R_{ij}^k R_{kl}^p dV + \int_V M_{ij}^k D_{ijkl} M_{kl}^p dV \ ,$$

which is also symmetric.

Similarly, the inertial terms, which are both symmetric are defined like

$$M_{uu}^{kp} = \rho \int_V {}_u N_i^k \ {}_u N_i^p dV$$
$$M_{\theta\theta}^{kp} = J_{ij} \int_V {}_\theta N_i^k \ {}_\theta N_j^p dV.$$

Finally, the external force and moment vector read

$$f_{ext}^p = \int_S {}_u N_i^p t_i dS \ ,$$
$$q_{ext}^p = \int_S {}_\theta N_i^p m_i dS \ .$$

4.3 Scattering of P waves by a semicircular canyon in a micropolar half-space

As an application of the numerical scheme described above and implemented through the user element subroutines (UEL) into the commercial code ABAQUS, we study the scattering of plane body waves by a semi-circular canyon in an elastic micro-polar half-space. In the case of a classical continuum, the problem has been previously solved by Kawase (1988) in the context of topographic effects in earthquake engineering using a boundary integral equation formulation with half-space Green's functions represented in the wave number domain. The same geometry, but under the incidence of SH waves, was addressed by Trifunac (1973), who found a solution in terms of expansions in eigenfunctions in a polar coordinate system. In both cases, the semi-circular canyon problem has become a benchmark solution to validate numerical methods and to develop fundamental understanding of topographic effects in earthquake engineering. For the case of non-classical media, like the current Cosserat micropolar model, there is no such a comprehensive study. The current work, although is not exhaustive constitutes a first approach to the scattering problem in a micro-polar medium. In this work the problem can be interpreted in a more general context depending on the values of the mechanical parameters selected for the micropolar model as will be described later.

The problem is first addressed in the frequency domain where we solve the system given in (2.4) for a discrete range of frequencies. Each solution step, for a given frequency, amounts to finding the steady state response for an incident plane wave of unit amplitude and frequency ω and with a time dependence of the form $e^{\hat{i}\omega t}$. Accordingly, the solution throughout the whole frequency range corresponds to the Fourier spectral response denoted like $U(\hat{i}\omega)$ and $V(\hat{i}\omega)$ for the horizontal and vertical fields respectively. In particular we are interested in the transfer function (TF) or ratio between the spectral response amplitude and that of the incident field. For instance, if the horizontal response is given by $U = U_R + \hat{i}U_I$, then the $U-$field transfer function is defined by the ratio of $\|U\| = [U_R^2 + U_I^2]^{1/2}$ to the amplitude of the incident wave. To find the time domain response, the incident plane wave is described by a Ricker pulse defined as $u(\tau) = (2\pi^2 f_c^2 \tau^2 - 1) exp(-\pi^2 f_c^2 \tau^2)$ where f_c = the nondimensional characteristic frequency of the pulse, τ = the nondimensional time $t\beta/a$ where t is the real time, a = the radius of the canyon and β = the classical shear wave propagation velocity. The final time domain response at a given point is obtained after inverse Fourier transforming the product of the response $\|u\|$ and the Fourier spectra for the pulse denoted by $R(\hat{i}\omega)$.

We solved the problem for $f_c = 1.0$ Hz, $f_{max} = 4.0$ Hz, $a = 1.0$ km, $\rho = 1.0$ kg/m^3, $\beta = 1.0$ km/s, $\mu_c = 1.0 \times 10^6$ N/m^2, $J = 3.33 \times 10^5$ kg/m, $\xi = 1.0 \times 10^{12}$ N and $\nu = 1/3$ and vertically incident P waves. The results are obtained using both, the classical and the micro-polar model. In order to give some preliminary interpretation of the results, it is convenient to describe the mechanical parameters in terms of the coupling number $N^2 = \mu_c/(\mu + \mu_c)$, which indicates the degree of coupling between the macro and micro-structure. When $N \to 0$ the micro-rotations occur independently of the macro-rotations and the relative stress term σ_{ij} is small; we refer to this case

as the uncoupled state. In contrast, a large value of N indicates a strong coupling between the micro-rotation and the macro-rotation, with large relative stresses. On the other hand, it is also convenient to introduce the concept of a length scale parameter describing the characteristic size of the micro-structure. Here we use as a length scale parameter $\ell^2 = \xi(\mu + \mu_c)/2\mu\mu_c$. We have selected a value corresponding to $\ell = a$ which is representative of the scattering by a defect (i.e., the cavity) with a characteristic dimension close to the microstructural length scale. As a first verification of the correctness of the implementation and of the model, we selected micro-polar parameters close to zero, so the classical solution could be recovered with the enriched model.

In Figure 4.2 the frequency domain results are shown in terms of spatial distributions for receivers along the cavity surface, of the transfer functions at the specific value of the dimensionless frequency $\eta = \omega a/\pi\beta \equiv 2a/\lambda = 2$. In the figure we show the results corresponding to the classical and micropolar model.

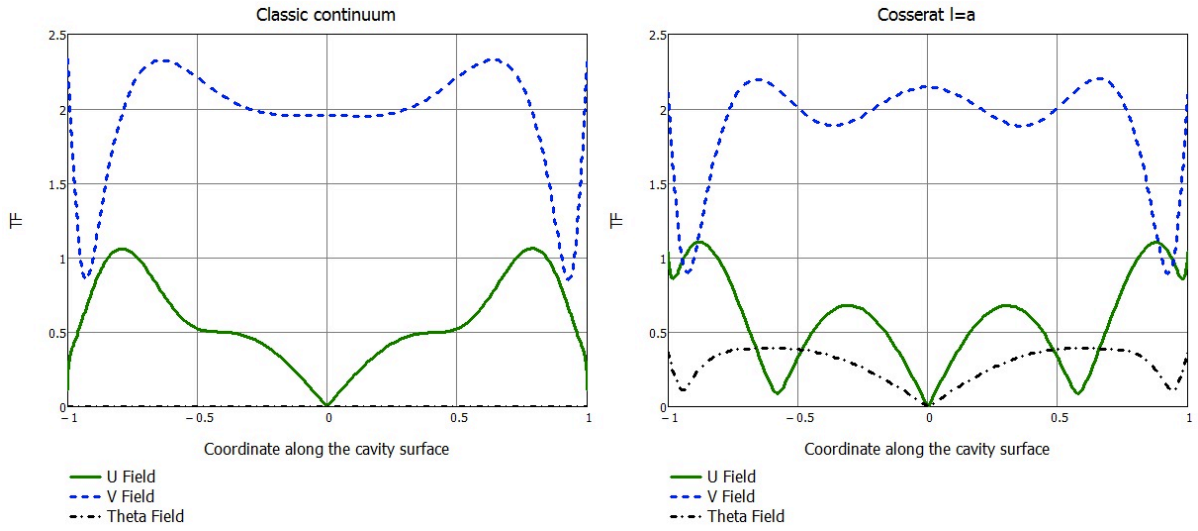

Figure 4.2. Spatial distribution of the transfer function along the cavity surface under vertically incident P waves.

A general observation from the obtained transfer functions, is the increase in the scattered component of the response due to the micro-structural effect. For instance, under vertically incident P waves the incident field is fully composed of vertical displacements, while the horizontal motion is completely generated by the scattered field. As a result of the micro-structural effects additional amplifications associated to the horizontal displacement component appear over the canyon surface as compared with the classical result. This is an expected result since the scattered field is mainly composed of shear waves which are precisely the ones affected by the micro-structural properties.

The solution in the time domain is presented in Figure 4.3, where the time histories along the cavity surface are shown. As already observed from the frequency domain response, the scattered component, corresponding in this case to the horizontal field experiences dispersion. This is observed by the distortion in the pulse as it propagates throughout the surface. At the

same time, the size or micro-structural effect result in reductions in the duration, since the P wave and the SV wave propagate in phase due to the increase in velocity of the shear wave.

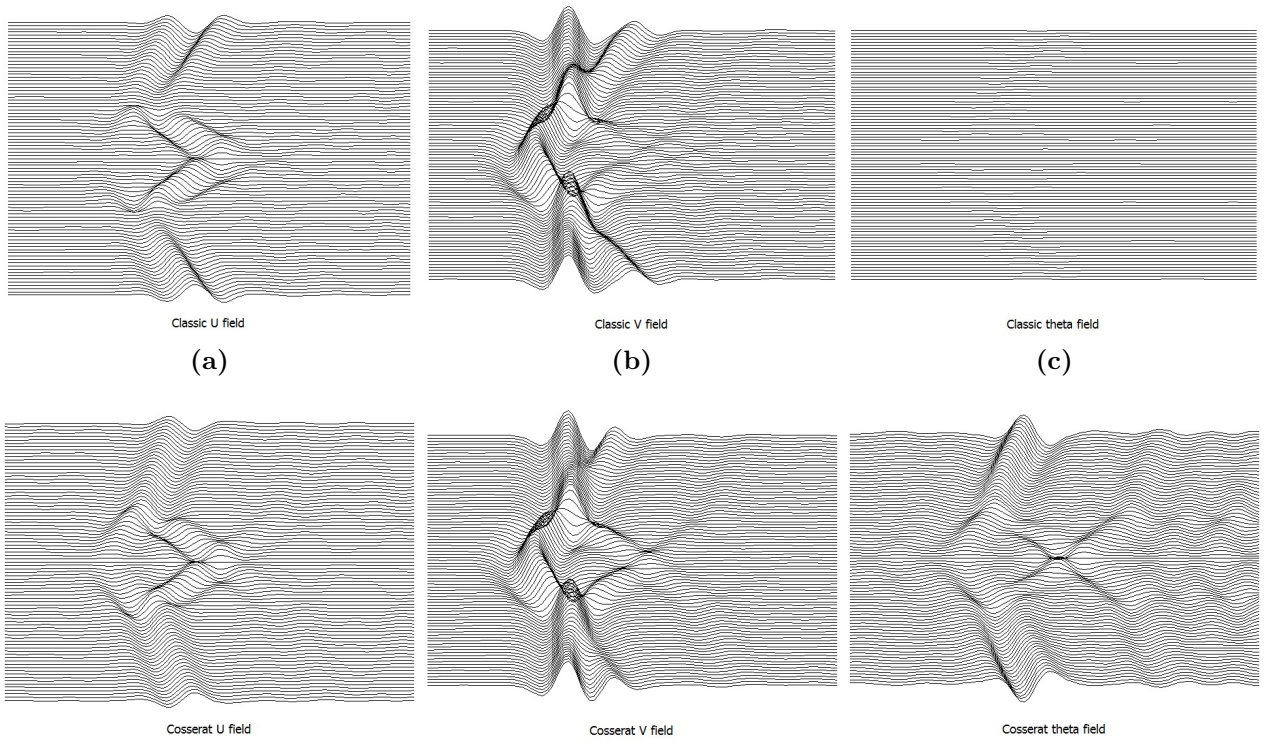

Figure 4.3. Synthetic seismograms for the semi-circular canyon in a micropolar half-space under vertically incident P waves.

A second analysis was performed with the same set of mechanical parameters but with a pulse characterized by a central frequency $f_c = 4.0$ Hz and a maximum frequency $f_{max} = 16.0$ Hz in order to increase the dispersion in the model. Figures 4.4 and 4.5 depict the complete transfer function and synthetic sesimograms for receivers over the canyon surface. Comparing the seismograms corresponding to the horizontal field (which is rich in scattered motions) it is clear how in the classical model the P and SV phases appear separated and propagating at different velocities. In the micropolar model both phases become a single one resulting in a reduction in the duration and frequency content of the response. Figure 4.6 displays snapshots of the propagation patterns over the computational domain for the classical and micropolar model. At t_1 the incident non-dispersive P waves have travelled the same distance and both pulses retain their original forms. At t_2 the incident wave has already been diffracted by the canyon free surface. In the classical case the diffracted P and SV waves are clearly identifiable. In the micropolar case however both phases are becoming to intercalate with one another as a result of the higher velocity of propagation in the shear wave. In the subsequent snapshots at t_3 and t_4, the separation between the diffracted P and SV waves grows, but at a higher rate in the classical model.

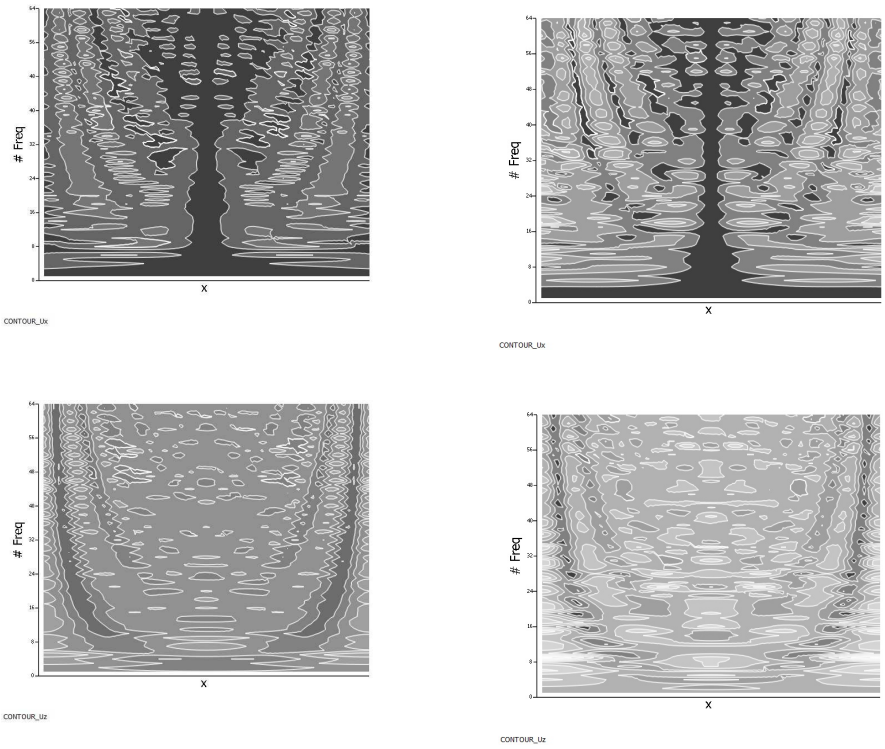

Figure 4.4. Frequency domain transfer functions for the classical canyon (left) and micro-polar canyon (right) for receivers over the canyon surface.

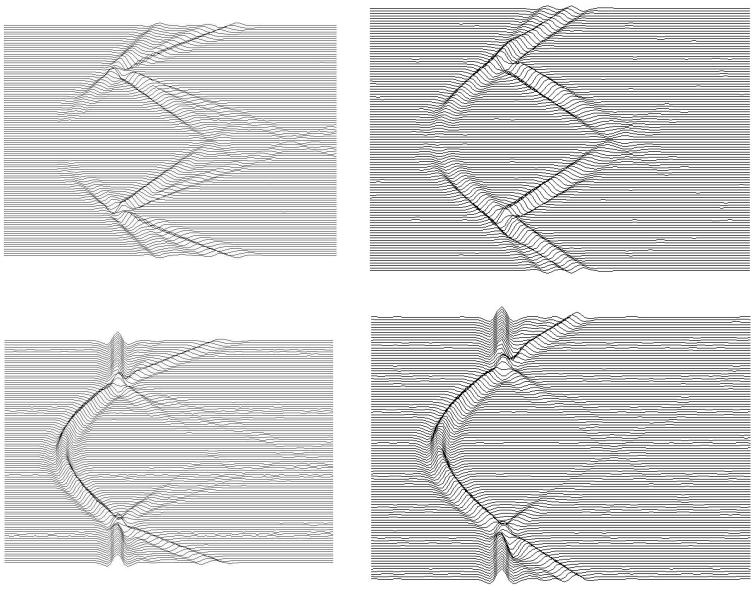

Figure 4.5. Synthetic seismograms for the horizontal and vertical fields over the semi-circular canyon surface with the classical material (left) and the micro-polar material (right).

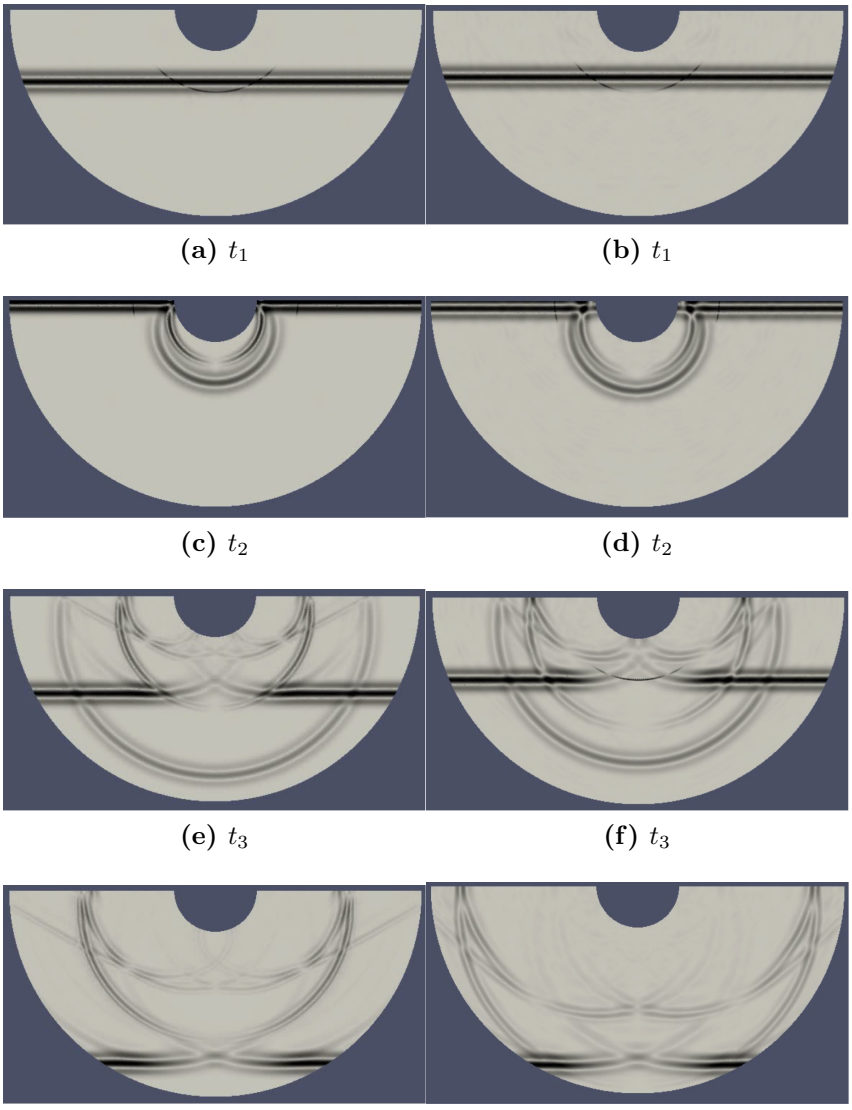

(a) t_1 **(b)** t_1

(c) t_2 **(d)** t_2

(e) t_3 **(f)** t_3

(g) t_4 **(h)** t_4

Figure 4.6. Snapshots of the propagation patterns in the semi-circular canyon with a classical model (left) and a micro-polar model (right). The full video is available at `http://www.youtube.com/watch?v=y-3j5BdTDaw&feature=youtu.be`

Conclusions and Further Work

Conclusions

The wave scattering problem in classical elastodynamics was reviewed and formulated both in differential and integral form. The formulation was described in terms of total motions inside the scatterer and relative or scattered motions inside the half-space.

A user element subroutine (UEL), to solve the scattering problem in a generalized wave propagation analysis over infinite and semi-infinite spaces in the frequency domain, has been implemented into the commercial finite element code ABAQUS. The subroutine overcomes the existing limitation of allowing only real-valued implementations in terms of user elements. This was achieved by treating the complex-valued problem as two separate real-valued problems, which independently account for the real and imaginary parts of the response. The subroutine can be used in everyday engineering practice with minimum data preparation.

The versatility of the subroutine was demonstrated by its application to solve mechanical wave scattering problems in a classical elastic model and in a non-classical micropolar model. Furthermore the subroutine can be easily extended to consider additional kinematic assumptions or even different physical contexts, like horizontally polarized shear waves or electromagnetic waves.

As application examples the UEL subroutine was applied to the solution to three different problems, as follows next.

Scattering in a micropolar model

The problem of scattering of vertically incident P waves by a semi-circular canyon supported by a micro-polar half-space was solved. In such a model the transverse SV waves behave dispersively leading to a different diffraction pattern as compared to the solution with a classical model. The consideration of a material micro-structure in this non-classical continuum model resulted in modifications to the frequency content of the response. In part this is due to the shear wave

propagation velocity exceeding the longitudinal wave propagation velocity for certain phases of the signal according to its frequency. As immediate future development of the subroutine, it must be extended to consider also incident shear waves. In the field of seismic engineering Cosserat models are known to be applicable to study rock mechanics, granular soils at high frequencies and recently in the study of what has been called rotational seismology. On the other hand, a natural and relevant question that can be addressed in the future with the aid of the user element subroutine, is related to the physical basis of the enriched or non-classical continuum models. This can be done via a wave propagation analysis of the material described with a Cosserat-like model and with a classical model, but considering the complete microstructural details.

The role of diffraction in the problem of site effects

By solving the two simple wave scattering problems of a semi-circular and a rectangular canyon, a method was proposed to separate the diffracted part of the response from the total solution. This diffracted component is expected to contain all the relevant information about the topographic effect and a preliminary analysis showed how the amplifications of the ground motions near these simple shapes, was connected to the diffracted field. It was identified that in order to advance in the development of this approach, the solution to some fundamental or canonical problems must be obtained first. For instance knowing and understanding the diffraction produced by a wedge is instrumental to reveal the physics behind the diffraction of in-plane waves. That solution would serve as analysis tool to interpret the results from complex geometries. Such solution must be obtained numerically.

The domain reduction method to study site effects

The domain reduction method proposed by Professor Jacobo Bielak at Carnegie Mellon University, was applied to study the idealization of seismic microzones over a sedimentary basin in the form of a canyon. For the canyon a cross section representative of those existing in the Valle de Aburrá was considered and two simple soil deposits or microzones were placed at extreme locations inside the canyon. The domain reduction method was used to capture, in a multi-step analysis, the regional geometric effect and to subsequently transfer it in the form of effective excitations to the different micro-zones. The obtained results suggest that the method is effective as analysis tool of the topographic effect in earthquake engineering and it will be further explored in the immediate future.

The commercial code ABAQUS together with the implemented UEL subroutine was used to solve problems as large as 6'000.000 degrees of freedom in 16Gb of memory desktop computer. This computational power is currently being used at the Mecanica Aplicada Lab to study the seismic response of gravity dams and other problems related to earthquake engineering.

The user subroutine, ABAQUS input files corresponding to sample problems and other related material can be downloaded freely from the Group's web site.

Appendix A

Sample Problem: Scattering by a Semicircular Canyon

As a verification, the transfer function for the dimensionless frequency $\eta = 1.0$ corresponding to a P wave vertically incident on a semi-circular canyon is presented in Figure A.1

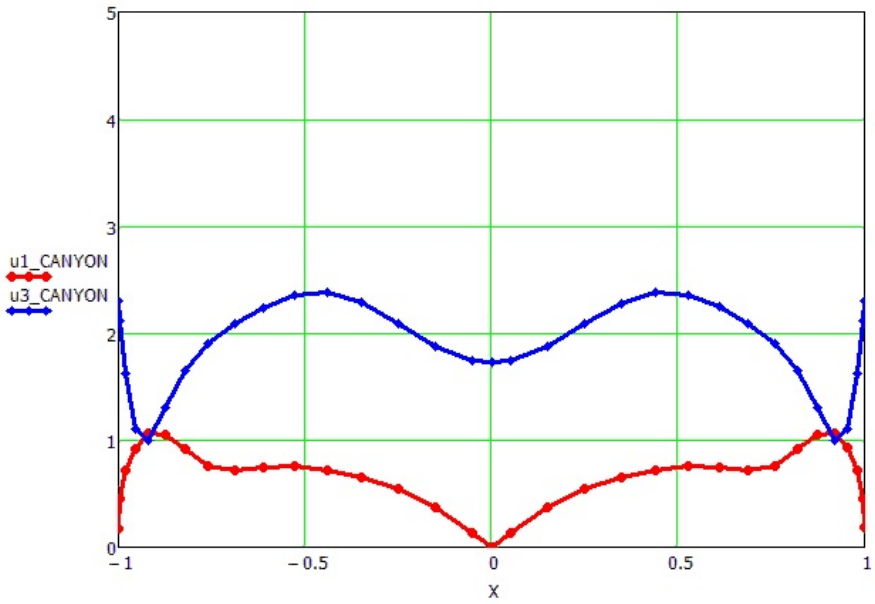

Figure A.1. Transfer function for the semi-circular canyon under vertically incident P wave.

these results correspond to the mesh shown in Figure A.2 and the input file together with the ABAQUS user element subroutine can be downloaded from the link `https://www.dropbox.com/sh/cl35rpynv6ynytf/qWCS4s21g1/CLASSIC%20UEL`.

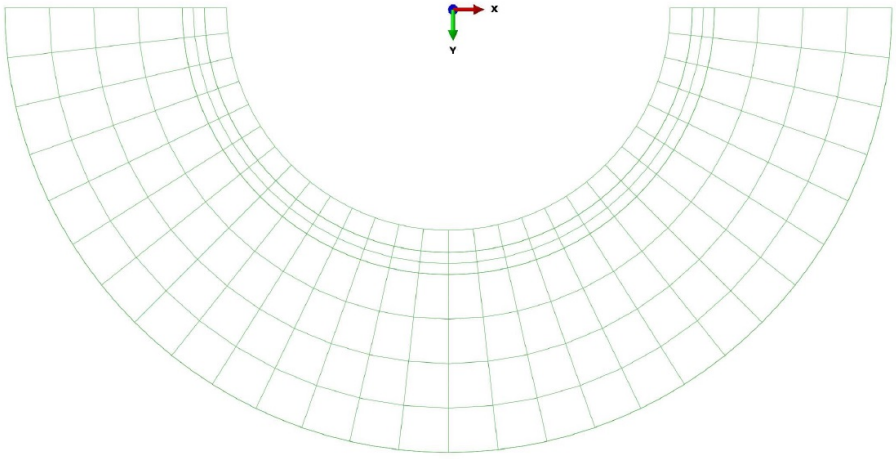

Figure A.2. Mesh for the semi-circular canyon under vertically incident P wave.

Bibliography

Aagaard, B. T. & Heaton, T. H., 2004. Near-source ground motions from simulations of sustained intersonic and supersonic fault ruptures, *Bulletin of the Seismological Society of America*, **94**(6), 2064–2078.

Achenbach, J., 1973. *Wave Propagation in Elastic Solids. Applied Mathematics and Mechanics*, North-Holland Publishing Company. Amsterdand-London.

Aero, E. & Kuvshinskii, E., 1961. Fundamental equations of theory of elastic media with rotationally interacting particles., *Soviet Physics Solid State*, **2**, 1272–1281.

Airman, T., 1972. Wave propagation in amicropolar elastic half-space, *Acta Mechanica*, **13**, 11–20.

Aki, K. & Richards, P., 2002. *Quantitative seismology*, Univ Science Books.

Archuleta, R. J. & Day, S. M., 1980. Dynamic rupture in a layered medium: the 1966 parkfield earthquake, *Bulletin of the Seismological Society of America*, **70**(3), 671–689.

Archuleta, R. J. & Frazier, G. A., 1978. Three-dimensional numerical simulations of dynamic faulting in a half-space, *Bulletin of the Seismological Society of America*, **68**(3), 541–572.

Banerjee, P., 1994. *The boundary element methods in engineering*, McGraw-Hill, London.

Bao, H., Bielak, J., Ghattas, O., Kallivokas, L., O'Hallaron, D., Shewchuk, J., & Xu, J., 1998. Large-scale simulation of elastic wave propagation in heterogeneous media on parallel computers, *Computer methods in applied mechanics and engineering*, **152**(1), 85–102.

Bielak, J. & Christiano, P., 1984. On the effective seismic input for non-linear soil-structure interaction systems, *Earthquake engineering & structural dynamics*, **12**(1), 107–119.

Bielak, J., Loukakis, K., Hisada, Y., & Yoshimura, C., 2003. Domain Reduction Method for Three-Dimensional Earthquake Modeling in Localized Regions, Part I: Theory, *Bulletin of the Seismological Society of America*, **93**, 817–824.

Bielak, J., MacCamy, R., McGhee, D., & Barry, A., 2009. Unified Symmetric BEM-FEM for Site Effects on Ground Motion â“ SH Waves, *Journal of Engineering Mechanics*, **117**, 2265–2285.

Bielak, J., Graves, R., Olsen, K., Taborda, R., Ramírez-Guzmán, L., Day, S., Ely, G., Roten, D., Jordan, T., Maechling, P., Urbanic, J., Cui, Y., & Juve, G., 2010. The ShakeOut earthquake scenario: Verification of three simulation sets, *Geophysical Journal International*, **180**, 375â“404.

Boore, D. M., 1972. A note on the effect of simple topography on seismic sh waves, *Bulletin of the Seismological Society of America*, **62**(1), 275–284.

Brockhouse, B. & Huang, K., 1958. Normal modes of germanium by neutron spectroscopy, *Physics Review*, pp. 747–754.

Chaljub, E., Capdeville, Y., & Vilotte, J.-P., 2003. Solving elastodynamics in a fluidâ“solid heterogeneous sphere: a parallel spectral element approximation on non-conforming grids, *Journal of Computational Physics*, **187**(2), 457 – 491.

Chaljub, E., Moczo, P., Tsuno, S., Bard, P.-Y., Kristek, J., Käser, M., Stupazzini, M., & Kristekova, M., 2010. Quantitative Comparison of Four Numerical Predictions of 3D Ground Motion in the Grenoble Valley, France, *Bulletin of the Seismological Society of America*, **100**(4), 1427â“1455.

Cosserat, E. & Cosserat, F., 1909. *Theorie des Corps Deformables.*, A Hermann et Fils.

Cowin, S., 1970. Stress functions for cosserat elasticity, *International Journal of Solids and Structures*, **6**(4), 389–398.

Cupillard, P., Delavaud, E., Burgos, G., Festa, G., Vilotte, J., Capdeville, Y., & Montagner, J., 2012. Regsem: a versatile code based on the spectral element method to compute seismic wave propagation at the regional scale, *Geophysical Journal International*.

Dravinski, M. & Mossessian, T., 1987. Scattering of plane harmonic p, sv, and rayleigh waves by dipping layers of arbitrary shape, *Bulletin of the Seismological Society of America*, **77**(1), 212–235.

Eringen, A., 1966. Linear theory of micropolar elasticity, *Journal of Mathematics and Mechanics*, **15**, 909–923.

Eringen, A. & Şuhubi, E., 1975. *Elastodynamics*, vol. 2, Academic press New York.

Faccioli, E., Maggio, F., Quarteroni, A., & Tagliani, A., 1996. Spectral-domain decomposition methods for the solution of acoustic and elastic wave equations, *Geophysics*, **61**(4), 1160–1174.

Frankel, A., 1993. Three-dimensional Simulations of Ground Motions in the San Bernardino Valley, California, for Hypotetical Earthquakes on the San Andreas Fault, *Bulletin of the Seismological Society of America*, **83**, 1020–1041.

Frankel, A. & Vidale, J., 1992. A three-dimensional simulation of seismic waves in the santa clara valley, california, from a loma prieta aftershock, *Bulletin of the Seismological Society of America*, **82**(5), 2045–2074.

Gazdag, J., 1981. Modeling of the acoustic wave equation with transform methods, *Geophysics*, **46**(6), 854–859.

Gazis, D. & Wallis, R., 1962. Extensional waves in cubic plates, in *Proceedings of the 4th U.S National Congress of Applied Mechanics*.

Gonella, S. & Ruzzene, M., 2007. Bridging scales analysis of wave propagation in heterogeneous structures with imperfections, *Wave Motion*, **45**, 481–497.

Graves, R. W., 1996. Simulating seismic wave propagation in 3d elastic media using staggered-grid finite differences, *Bulletin of the Seismological Society of America*, **86**(4), 1091–1106.

Ichimura, T., Hori, M., & Kuwamoto, H., 2007. Earthquake motion simulation with multiscale finite-element analysis on hybrid grid, *Bulletin of the Seismological Society of America*, **97**(4), 1133–1143.

Igel, H., Cochard, A., Wassermann, J., Flaws, A., Ulrich, S., Schreiber, S., Velikoseltsev, A., & Pham, N., 2007. Broadband observations of earthquake-induced rotational ground motions, *Geophysical Journal International*, **168**, 182–196.

Ignaczak, J., 1972. Radiation conditions in asymmetric elasticity., *Journal of Elasticity*, **2**, 307–321.

Iturrarán-Viveros, U., Vai, R., & Sánchez-Sesma, F., 2005. Scattering of elastic waves by a 2-D crack using the Indirect Boundary Element Method (IBEM)., *Geophysical Journal International,*, **162**, 927–934.

Iturrarán-Viveros, U., Vai, R., & Sánchez-Sesma, F. J., 2010. Diffraction of sh cylindrical waves by a finite crack: an analytical solution, *Geophysical Journal International*, **181**(3), 1634–1642.

Janod, F. & Coutant, O., 2000. Seismic response of three-dimensional topographies using a time-domain boundary element method, *Geophysical Journal International*, **603-614**, 142.

Jaramillo, J., Gomez, J., Saenz, M., & Vergara, J., 2013. Analytic approximation to the scattering of antiplane shear waves by free surfaces of arbitrary shape via superposition of incident, reflected and diffracted rays, *Geophysical Journal International*, **192**(3), 1132–1143.

Kawase, H., 1988. Time domain response of a semicircular canyon for incident sv, p, and rayleigh waves calculated by the discrete wavenumber boundary element method, *Bulletin of the Seismological Society of America*, **78**, 1415–1437.

Kawase, H. & Aki, K., 1989. A study on the response of a soft basin for incident s, p, and rayleigh waves with special reference to the long duration observed in mexico city, *Bulletin of the Seismological Society of America*, **79**(5), 1361–1382.

Kawase, H. & Aki, K., 1990. Topography effect at the critical sv-wave incidence: possible explanation of damage pattern by the whittier narrows, california, earthquake of 1 october 1987, *Bulletin of the Seismological Society of America*, **80**(1), 1–22.

Keller, J., 1956. Diffraction by a convex cylinder, *IEEE Transactions on Antennas and Propagation., AP-24*, **AP-24**, 312–321.

Keller, J., 1957. Diffraction by an aperture, *Journal of Applied Physics*, **28**(4), 426–444.

Keller, J., 1962. Geometrical theory of diffraction, *Journal of the Optical Society America*, **52**(2), 116–130.

Khan, S., Dhaliwal, R., & Chowdhury, K., 1971. Singular solutions and green's method in micropolar theory of elasticity, *Appl.Sci.Res*, **25**, 65–82.

Kim, J. & Papageorgiou, A., 1993. Discrete wave-number boundary-element method for 3-d scattering problems, *Journal of engineering mechanics*, **119**(3), 603–624.

Koiter, W., 1964. Couple stresses in the theory of elasticity, *Proc.K.Ned.Akad.Wet(B)*, **67**, 17–44.

Komatitsch, D. & Tromp, J., 1999. Introduction to the spectral element method for three-dimensional seismic wave propagation, *Geophysical Journal International*, **139**(3), 806–822.

Komatitsch, D. & Vilotte, J., 1998. The spectral element method: An efficient tool to simulate the seismic response of 2d and 3d geological structures, *Bulletin of the Seismological Society of America*, **88**(2), 368–392.

Komatitsch, D., Liu, Q., Tromp, J., Süss, P., Stidham, C., & Shaw, J. H., 2004. Simulations of Ground Motion in the Los Angeles Basin Based upon the Spectral-Element Method, *Bulletin of the Seismological Society of America,*, **94**(1), 187â“206.

Kosloff, D. & Baysal, E., 1982. Forward modeling by a fourier method, *Geophysics*, **47**(10), 1402–1412.

Kouyoumjian, R. & Pathak, P., 1974. A uniform geometrical theory of diffraction for an edge in a perfectly conducting surface., *Proceedings of the IEEE*, **62**(11), 1448–1461.

Kulesh, M., 2006. Rayleigh-type waves for the isotropic elastic reduced cosserat half-space. application in rocks and soils.

Kulesh, M., Matveenko, V. P., & Shardakov, I. N., 2005. Construction and analysis of an analytical solution for the surface rayleigh wave within the framework of the cosserat continuum, *Journal of Applied Mechanics and Technical Physics*, **46**, 556â“563.

Kulesh, M., Matveenko, V. P., & Shardakov, I. N., 2006. Propagation of surface elastic waves in the cosserat medium, *Acoustical Physics*, **52**, 227–235.

Lakes, R., 1982. Dynamical study of couple stress effects in human compact bone, *Journal of Biomechanical Engineering*, **104**, 6–10.

Lee, C.-H., Kihou, K., Horigane, K., Tsutsui, S., Fukuda, T., Eisaki, H., Iyo, A., Yamaguchi, H., Baron, A. Q. R., Braden, M., & Yamada, K., 2010. Effect of K Doping on Phonons in Ba_{1-x} K_x Fe_2 As_2, *Journal of the Physical Society of Japan*, **79**, 014714.

Lee, S.-J., Chan, Y.-C., Komatitsch, D., & Tromp, B.-S. H. J., 2009a. Effects of Realistic Surface Topography on Seismic Ground Motion in the Yangminshan Region of Taiwan Based Upon the Spectral-Element Method and LiDAR DTM, *Bulletin of the Seismological Society of America*, **99**(2), 681–693.

Lee, S.-J., Komatitsch, D., Huang, B.-S., & Tromp, J., 2009b. Effects of Topography on Seismic-Wave Propagation: An Example from Northern Taiwan, *Bulletin of the Seismological Society of America*, **99**(1), 314–325.

Levander, A. R., 1988. Fourth-order finite-difference p-sv seismograms, *Geophysics*, **53**(11), 1425–1436.

Love, A. E. H., 2013. *A treatise on the mathematical theory of elasticity*, Cambridge University Press.

Lysmer, J. & Drake, L. A., 1972. A finite element method for seismology, *Methods in computational physics*, **11**, 181–216.

Ma, S. & Liu, P., 2006. Modeling of the perfectly matched layer absorbing boundaries and intrinsic attenuation in explicit finite-element methods, *Bulletin of the Seismological Society of America*, **96**(5), 1779–1794.

MacDonald, H., 1902. *Electric Waves*, Cambridge University Press.

Madariaga, R., 1977. High-frequency radiation from crack (stress drop) models of earthquake faulting, *Geophysical Journal of the Royal Astronomical Society*, **51**(3), 625–651.

Maday, Y. & Patera, A. T., 1989. Spectral element methods for the incompressible Navier-Stokes equations, in *State-of-the-art surveys on computational mechanics (A90-47176 21-64). New York, American Society of Mechanical Engineers, 1989, p. 71-143. Research supported by DARPA.*, pp. 71–143.

Manolis, G. & Beskos, D., 1988. *Boundary Element Methods in Elastodynamics*, Spon Press, 1st edn.

Midya, G., 2004. On love-type surface waves in homogeneous micropolar elastic media, *International Journal of Engineering Science*, **42**, 1275–1288.

Mindlin, R., 1964. Micro-structure in linear elasticity, *Archives of Rational Mechanics and Analysis*, **16**, 51–78.

Mindlin, R., 1965. Second gradient of strain and surface tension in linear elasticity, *International Journal of Solids and Structures*, **1**, 417–438.

Mindlin, R. & Eshel, N., 1965. On first strain gradient theories in elasticity, *International Journal of Solids and Structures*, **4**, 119–124.

Mindlin, R. & Tiersten, H., 1963. Effects of couple-stresses in linear elasticity, *Archives of Rational Mechanics and Analysis*, **11**, 415–448.

Mita, A. & Luco, J. E., 1987. Dynamic response of embedded foundations: a hybrid approach, *Computer methods in applied mechanics and engineering*, **63**(3), 233–259.

Moczo, P., Robertsson, J. O., & Eisner, L., 2007. The finite-difference time-domain method for modeling of seismic wave propagation, *Advances in Geophysics*, **48**, 421–516.

Mossessian, T. & Dravinski, M., 1989. Scattering of elastic waves by three-dimensional surface topographies, *Wave motion*, **11**(6), 579–592.

Mow, C.-C. & Pao, Y.-H., 1971. *The diffraction of elastic waves and dynamic stress concentrations*, Rand Corporation.

Ohtsuki, A. & Harumi, K., 1983. Effect of topography and subsurface inhomogeneities on seismic sv waves, *Earthquake Engineering & Structural Dynamics*, **11**(4), 441–462.

Okamoto, T., Takenaka, H., Nakamura, T., & Aoki, T., 2011. Large-scale simulation of seismic-wave propagation of the 2011 tohoku-oki m9 earthquake, in *Proceedings of the International Symposium on Engineering Lessons Learned from the*, pp. 349–360.

Olsen, K. B. & Archuleta, R. J., 1996. Three-dimensional simulation of earthquakes on the los angeles fault system, *Bulletin of the Seismological Society of America*, **86**(3), 575–596.

Orszag, S., 1980. Spectral methods for problems in complex geometries, *Journal of Computational Physics*, **37**(1), 70–92.

Pao, Y. H. & Varatharajulu, V., 1976. Huygens principle, radiation conditions, and integral formulas for the scattering of elastic waves, *The Journal of the Acoustical Society of America*, **59**(6), 1361–1371.

Papageorgiou, A. S. & Pei, D., 1998. A discrete wavenumber boundary element method for study of the 3-d response 2-d scatterers, *Earthquake engineering & structural dynamics*, **27**(6), 619–638.

Papargyri-Beskou, S., Polyzos, A., & Beskos, D., 2009. Wave dispersion in gradient elastic solids and structures: A unified treatment, *International Journal of Solids and Structures*, **46**, 3751–3759.

Parfitt, V. & Eringen, A., 1969. Reflection of plane waves from the flat boundary of a micro-polar elastic half-space, *Journal of the Acoustical Society of America*, pp. 1258–1272.

Patera, A. T., 1984. A spectral element method for fluid dynamics: Laminar flow in a channel expansion, *Journal of Computational Physics*, **54**, 468 – 488, This was the first paper in Spectral Element Methods.

Priolo, E., Carcione, J., & Seriani, G., 1994. Numerical simulation of interface waves by high-order spectral modeling techniques, *The Journal of the Acoustical Society of America*, **95**, 681.

Restrepo, D., Taborda, R., & Bielak, J., 2012. Three-dimensional nonlinear earthquake ground motion simulation in the salt lake basin using the wasatch front community velocity model.

Sanchez-Sesma, F., 1985. Diffraction of elastic sh waves by wedges, *Bulletin of the Seismological Society of America*, **75**(5), 1435–1446.

Sánchez-Sesma, F. & Campillo, M., 1991. Diffraction of P, SV, and Rayleigh waves by topographic features: A boundary integral formulation, *Bulletin of the Seismological Society of America*, **81**(6), 2234–2253.

Sanchez-Sesma, F. & Iturraran-Viveros, U., 2001. Scattering and diffraction of sh waves by a finite crack: an analytical solution, *Geophysical Journal International*, **145**, 749–758.

Sánchez-Sesma, F. J., 1983. Diffraction of elastic waves by three-dimensional surface irregularities, *Bulletin of the Seismological Society of America*, **73**(6A), 1621–1636.

Sánchez-Sesma, F. J. & Iturrarán-Viveros, U., 2001. Scattering and diffraction of sh waves by a finite crack: an analytical solution, *Geophysical Journal International*, **145**(3), 749–758.

Sánchez-Sesma, F. J. & Rosenblueth, E., 1979. Ground motion at canyons of arbitrary shape under incident sh waves, *Earthquake Engineering & Structural Dynamics*, **7**(5), 441–450.

Smith, W. D., 1975. The application of finite element analysis to body wave propagation problems, *Geophysical Journal of the Royal Astronomical Society*, **42**(2), 747–768.

Sohrabi-Bidar, A., Kamalian, M., & Jafari, M. K., 2010. Seismic response of 3-d gaussian-shaped valleys to vertically propagating incident waves, *Geophysical Journal International*, **183**(3), 1429–1442.

Sommerfeld, A., 1896. Mathematische theorie der diffraktion., *Math.Ann*, **47**, 317–374.

Stekl, I. & Pratt, R. G., 1998. Accurate viscoelastic modeling by frequency-domain finite differences using rotated operators, *Geophysics*, **63**(5), 1779–1794.

Taborda, R. & Bielak, J., 2010. Three dimensional nonlinear soil and site-city effects in urban regions.

Taborda, R. & Bielak, J., 2011. Large-scale earthquake simulation: Computational seismology and complex engineering systems, *Computing in Science & Engineering*, **13**(4), 14–27.

Takeo, M., 1998a. Ground rotational motions recorder in near-source region of earthquakes., *Geophysical Research Letters*, **25**, 789–792.

Takeo, M., 1998b. Ground rotational motions recorder of earthquakes., *Geophysical Research Letters.*, **Vol 26**, 789–792.

Takeo, M. & Ito, H., 1997. What can be learned from rotational motions excited by earthquakes?, *International journal of Geophyisics*, **129**, 319–329.

Teisseyre, R. & Gorski, M., 2009. Fundamental deformations in asymmetric continuum, *Bulletin of the Seismological Society of America*, **99**, 1132–1136.

Tomar, S. & Cogna, M., 1995. Reflection and refraction of longitudinal wave at an interface between two micropolar elastic solids in welded contact., *Journal of the Acoustical Society of America*, **97**, 822–830.

Tomar, S., Kumar, R., & Kaushik, V., 36. Wave propagation of micropolar elastic medium with stretch, *International Journal of Engineering Science*, **1998**, 683–698.

Toshinawa, T. & Ohmachi, T., 1992. Love-wave propagation in a three-dimensional sedimentary basin, *Bulletin of the Seismological Society of America*, **82**(4), 1661–1677.

Toupin, 1962. Elastic materials with couple-stresses, *Archives of Rational Mechanics andAnalysis*, **11**, 385–414.

Trifunac, M., 1973. Scattering of plane sh waves by a semi-cylindrical canyon., *Earthquake Engineering and Structural Dynamics*, **1**, 267–281.

Truesdell, C. & Toupin, R., 1960. *Principles of Classic Mechanics and Field Theory. Encyclopedia of Physics.*, Springer-Verlag.

Twiss, R., Souter, B., & Unrhu, J., 1993. The effect of block rotations on the global seismic moment tensors and the patterns of seismic p and t axes, *Journal of Geophysical Research*, **98**, 645–674.

Vidale, J. E. & Helmberger, D. V., 1988. Elastic finite-difference modeling of the 1971 san fernando, california earthquake, *Bulletin of the Seismological Society of America*, **78**(1), 122–141.

Virieux, J., 1986. P-sv wave propagation in heterogeneous media: Velocity-stress finite-difference method, *Geophysics*, **51**(4), 889–901.

Voigt, W., 1910. *Lehrbuch der Kristalphysik*, Teubner, B.

Wong, H., 1982. Effect of surface topography on the diffraction of p, sv, and rayleigh waves, *Bulletin of the Seismological Society of America*, **72**(4), 1167–1183.

Wong, H. & Jennings, P., 1975. Effects of canyon topography on strong ground motion, *Bulletin of the Seismological Society of America*, **65**(5), 1239–1257.

Yomogida, K. & Etgen, J. T., 1993. 3-d wave propagation in the los angeles basin for the whittier-narrows earthquake, *Bulletin of the Seismological Society of America*, **83**(5), 1325–1344.

Yoshimura, C., Hisada, J. B. Y., & Fernández, A., 2003. Domain Reduction Method for Three-Dimensional Earthquake Modeling in Localized Regions, Part II: Verification and Applications, *Bulletin of the Seismological Society of America*, **93**, 825–841.

Zhang, C. & Achenbach, J., 1988. A new boundary integral equation formulation for elastodynamic and elastostatic crack analysis., Tech. rep., DTIC Document.